A TOPBP1 Allele Causing Male Infertility Uncouples XY Silencing Dynamics From Sex Body Formation

Carolline F. R. Ascencao[1*], Jennie R. Sims[1*], Alexis Dziubek[1], William Comstock[1], Elizabeth A. Fogarty[1], Jumana Badar[1], Raimundo Freire[2,3,4], Andrew Grimson[1], Robert S. Weiss[5], Paula E. Cohen[5,#] and Marcus Smolka[1,#]

1. Department of Molecular Biology and Genetics, Cornell University, United States;
2. Fundación Canaria del Instituto de Investigación Sanitaria de Canarias (FIISC), Unidad de Investigación, Hospital Universitario de Canarias, La Laguna, Santa Cruz de Tenerife, Spain;
3. Instituto de Tecnologías Biomédicas, Universidad de La Laguna, 38200 La Laguna, Spain;
4. Universidad Fernando Pessoa Canarias, Las Palmas de Gran Canaria, Spain;
5. Department of Biomedical Sciences, Cornell University, United States.

* Contributed equally

\# Co-corresponding authors

ABSTRACT

Meiotic sex chromosome inactivation (MSCI) is a critical feature of meiotic prophase I progression in males. While the ATR kinase and its activator TOPBP1 are key drivers of MSCI within the specialized sex body (SB) domain of the nucleus, how they promote silencing remains unclear given their multifaceted meiotic functions that also include DNA repair, chromosome synapsis and SB formation. Here we report a novel mutant mouse harboring mutations in the TOPBP1-BRCT5 domain. *Topbp1*$^{B5/B5}$ males are infertile, with impaired MSCI despite displaying grossly normal events of early prophase I, including synapsis and SB formation. Specific ATR-dependent events are disrupted including phosphorylation and localization of the RNA:DNA helicase Senataxin. *Topbp1*$^{B5/B5}$ spermatocytes initiate, but cannot maintain ongoing, MSCI. These findings reveal a non-canonical role for the ATR-TOPBP1 signaling axis in MSCI dynamics at advanced stages in pachynema and establish the first mouse mutant that separates ATR signaling and MSCI from SB formation.

Introduction

During Prophase I, the SPO11 topoisomerase-like enzyme and its cofactors induce programmed DNA double-strand breaks (DSBs) that are then recognized by the DNA damage response (DDR) machinery to promote recombination between homologous chromosomes (Handel and Schimenti, 2010; Joshi et al., 2015; Keeney et al., 1997; Subramanian and Hochwagen, 2014). Proper chromosome synapsis achieved through the formation of the proteinaceous synaptonemal complex, together with homologous recombination (HR)-mediated DNA repair (Pereira et al., 2020) are critical for the formation of crossovers that ensure the correct segregation of chromosomes and the formation of healthy and genetically diverse haploid gametes (Gray and Cohen, 2016). Chromosomes that fail to synapse as prophase I progresses trigger a process referred to as meiotic silencing of unsynapsed chromatin (MSUC) (Abe et al., 2020; Burgoyne et al., 2009; Turner, 2015; Turner et al., 2006) to silence genes at unsynapsed regions. In the heterogametic sex (male mammals), the X and Y chromosomes pose a unique challenge for meiotic progression since they bear homology only at the pseudoautosomal region (PAR). The non-homologous arms of the sex chromosomes remain unsynapsed and must therefore undergo a sex-chromosome specific manifestation of MSUC, termed meiotic sex-chromosome inactivation (MSCI) (Alavattam et al., 2018; Royo et al., 2010; Turner, 2007; Turner et al., 2006). MSCI is critical for normal prophase I progression through two complementary mechanisms, the silencing of toxic Y-linked genes, such as *Zfy1* and *Zfy2*, that enforce the pachytene checkpoint (Royo et al., 2010; Vernet et al., 2016) and through the accumulation of the DDR machinery at the X and Y chromosomes, away from the autosomes, during early pachynema (Abe et al., 2020).

The apical serine-threonine kinase Ataxia Telangiectasia mutated and Rad-3 related (ATR), is a master regulator of DNA repair, checkpoints and silencing during prophase I in spermatocytes. In response to DSBs and asynapsis, ATR activation promotes a range of downstream effects, including recombinational DNA repair, crossing over, chromosome synapsis, cell cycle arrest and potentially apoptosis (Abe et al., 2022; Pacheco et al., 2018; Pereira et al., 2020; Royo et al., 2013; Widger et al., 2018). During leptonema and zygonema, shortly after DSB formation, ATR and its cofactor ATRIP are recruited to RPA-coated regions of single strand DNA (ssDNA) that accumulate upon 5’-3’ resection of both ends of DSBs (Cimprich and Cortez, 2008; Fanning et al.,

2006). ATR activation requires recruitment of TOPBP1 (topoisomerase 2 binding protein 1), a multi-BRCT (BRCA C-terminus motif) domain protein that stimulates ATR kinase activity through its ATR-activation domain (AAD) (Cimprich and Cortez, 2008; Kumagai et al., 2006; Mordes et al., 2008; Zhou et al., 2013). In addition to activating ATR, TOPBP1 also serves as a scaffold for a range of DDR factors, interacting with, and often recruiting them via its multiple BRCT domains (Bigot et al., 2019; Blackford et al., 2015; Cescutti et al., 2010; Delacroix et al., 2007; Leimbacher et al., 2019; Leung et al., 2011; Liu et al., 2017; Pereira et al., 2022). TOPBP1 is composed of nine BRCT domains, which are protein-interacting modules that typically recognize phosphorylated motifs (Liu et al., 2017; Manke et al., 2003; Rodriguez et al., 2003). Through the recognition of phosphoproteins, TOPBP1 is able to assemble multisubunit complexes to promote discrete pathways (Bigot et al., 2019; Blackford et al., 2015; Cescutti et al., 2010; Delacroix et al., 2007; ElInati et al., 2017; Jeon et al., 2019; Leimbacher et al., 2019; Leung et al., 2011; Liu et al., 2017; Pereira et al., 2022, 2020; Perera et al., 2004). TOPBP1 interacts with the C-terminal tail of RAD9, a component of the 9-1-1 PCNA-like clamp that is loaded at 5' recessed junctions adjacent to DSBs (Parrilla-Castellar et al., 2004). The 9-1-1-TOPBP1 complex is essential for canonical ATR signaling during prophase I (ElInati et al., 2017; Jeon et al., 2019; Perera et al., 2004). The interaction of proteins with TOPBP1 may facilitate their phosphorylation by ATR, suggesting a role for TOPBP1 in the control of ATR substrate selection.

As cells progress from zygonema into pachynema, ATR and TOPBP1 localize to the unsynapsed axes of the X and Y chromosomes (Broering et al., 2014; Moens et al., 1999; Reini et al., 2004), leading to phosphorylation of the histone variant H2AX on serine 139 (γH2AX), a major hallmark of MSCI (Royo et al., 2013; Widger et al., 2018). During establishment of MSCI, a phase separated structure termed the sex body is formed (Monesi, 1965; Solari, 1974; Xu and Qiao, 2021), allowing the confinement of ATR signaling, DDR factors and silencing to the X and Y (Abe et al., 2020; Turner, 2007) as part of a checkpoint that may induce cell death if DDR proteins aberrantly accumulate and remain on autosomes (Abe et al., 2020). Recruitment of ATR and TOPBP1 to unsynapsed regions of the XY requires a distinct set of factors compared to their mode of recruitment to autosomal DSB sites mentioned above, and involves factors such as BRCA1 and HORMAD (Shin et al., 2010; Turner et al., 2004). Activated ATR phosphorylates H2AX at the unsynapsed cores of the X and Y chromosomes, a signaling that is propagated to chromatin loops

of the X and Y, via a feed-forward process mediated by recruitment of the MDC1 adaptor, which further recruits and mobilizes additional TOPBP1-ATR complexes, therefore spreading ATR signaling to promote the broad chromosome-wide silencing required for MSCI (Ichijima et al., 2011). It has also been proposed that the initiation of MSCI accumulates DDR proteins from autosomes to the X and Y chromosomes to prevent excessive DDR signaling at autosomes from activating cellular checkpoints that can stop meiotic progression (Abe et al., 2020).

Despite mounting evidence pointing to the importance of ATR and TOPBP1 for MSCI, the precise mechanisms by which they promote sex body formation and XY silencing remain unknown. Moreover, it remains unclear how these two processes are spatiotemporally coordinated and how ATR and TOPBP1 mediate such coordination. Since both proteins are essential for organismal viability (Brown and Baltimore, 2000; De Klein et al., 2000; Jeon et al., 2011; O'Driscoll, 2009; O'Driscoll et al., 2007; Yamane et al., 2002; Zhou et al., 2013), conditional knockouts (ElInati et al., 2017; Royo et al., 2013; Widger et al., 2018) or hypomorphic (Pacheco et al., 2018) models have been used to explore their roles during prophase I in spermatocytes. However, given the strong pleiotropic effects in these models, especially in DSB repair, synapsis, MSCI and sex body formation, it is difficult to dissect the distinct molecular mechanisms involved, and to untangle direct versus indirect effects. Here we present a separation-of-function mouse mutant that deconvolutes TOPBP1-dependent ATR signaling in male meiosis. We generated mice bearing multiple mutations in BRCT-domain 5 (*Topbp1*$^{B5/B5}$ mice) that are viable and grossly indistinguishable from wild-type littermates; yet, the males are sterile, having reduced testes size, reduced seminiferous tubule cellularity, and a complete loss of sperm. Strikingly, while *Topbp1*$^{B5/B5}$ spermatocytes fail to progress into diplotene, they display largely normal chromosome synapsis, sex body formation, recruitment of DDR proteins to the X and Y, and DNA repair during prophase I, in sharp contrast to previous models of TOPBP1 or ATR impairment (ElInati et al., 2017; Widger et al., 2018). Single-cell RNA sequencing data showed that while MSCI is initiated in *Topbp1*$^{B5/B5}$, the dynamics of silencing progression and reinforcement is defective, which is accompanied by a defect in the localization of the RNA:DNA helicase Senataxin to chromatin loops of the XY chromosomes. We propose that the *Topbp1*$^{B5/B5}$ is a separation of function mutant that allows the untangling of XY silencing from sex body formation and DDR recruitment to the

XY, representing a unique model to study the establishment, maintenance, reinforcement and progression of MSCI.

Results

A TOPBP1 mutant separating its role in fertility from organismal viability.

Topbp1 knockout mice exhibit strong defects early in embryonic development, reaching blastocyst stage but not progressing beyond E.8, with embryos likely dying at the preimplantation stage (Jeon et al., 2011). In the context of meiosis, conditional knockout of *Topbp1* in spermatocytes leads to pleiotropic effects, including defects in chromosome synapsis, impaired recruitment of DDR factors to XY chromosomes, defects in condensation of the XY chromosomes, abnormal formation of the sex body, lack of γH2AX spreading to chromatin loops, all of which contribute to a strong MSCI defect as indicated by the complete absence of downstream markers of MSCI, such as USP7, H3K9me3, poly-ubiquitination and sumoylation (ElInati et al., 2017; Pereira et al., 2020). The availability of a separation of function mutant for *Topbp1* is therefore needed to dissect its distinct roles in development, organismal maintenance, and multiple meiotic processes such as DNA repair, silencing and sex body formation. To generate a separation of function mouse model, we inserted eight charge reversal point mutations in BRCT domain 5 of TOPBP1 (hereafter referred to as *Topbp1*$^{B5/B5}$) CRISPR/Cas9 (Figure 1A). After validating the point mutations through Sanger sequencing, (Supplemental Figure 1), we found that *Topbp1*$^{B5/B5}$ mice were viable, with no difference in body mass when compared to *WT* littermates (Figures 1B and 1C), and no sensitivity to Ionizing Radiation (IR) (Figures 1D). Strikingly, *Topbp1*$^{B5/B5}$ mice displayed male-specific infertility (Figure 1E), with a three-fold reduction in testis size (Figures 1F and 1G) and complete lack of spermatozoa (Figure 1H). H&E-stained histological testis sections revealed mainly spermatogonia and spermatocytes within the seminiferous epithelium (Figure 1I) together with an increased number of TUNEL-positive spermatocytes in seminiferous tubules (Figure 1J and 1K). Cytological evaluation of surface-spread spermatocytes from *Topbp1*$^{B5/B5}$ revealed the presence of meiotic prophase I stages from leptonema to pachynema but a total absence of diplonema-staged spermatocytes (Figure 1L). Moreover, the staining of the synaptonemal complex proteins SYCP1 and SYCP3 revealed normal pachytene entry and no gross defects in chromosome synapsis, distinct from previous models of ATR and TOPBP1 conditional depletion (ElInati et al., 2017; Widger et al., 2018). Furthermore, unlike reported DDR CKO (conditional knockouts) models such as *Rad1* and *Brca1* (Abe et al., 2020; Broering et al., 2014; Pereira et al., 2022), *Topbp1*$^{B5/B5}$

pachytene spermatocytes reach mid-pachynema, as demonstrated by the accumulation of signal for H1t (Inselman et al., 2003) (Figure 1L).

$Topbp1^{B5/B5}$ MEFs display no detectable DDR defects.

To assess the possibility of a somatic phenotype we derived mouse embryonic fibroblasts (MEFs) from $Topbp1^{B5/B5}$ and wild-type littermates at embryonic day E13.5. Consistent with the observed organismal viability and the lack of IR sensitivity, $Topbp1^{B5/B5}$ MEFs showed no sensitivity to hydroxyurea (replication stress) or phleomycin (DSBs) in a long-term cell survival assay (Figure 2A-D and Supplemental Figure 2). Genotoxic stress activates the apical kinases ATR, ATM and DNA-PKcs (Blackford and Jackson, 2017; Falck et al., 2005; Maréchal and Zou, 2013) to trigger a signaling cascade that promotes DNA repair and cell cycle arrest via activation of the downstream checkpoint kinases CHK1 and CHK2 (Hartwell and Kastan, 1994; Lanz et al., 2019; Shiloh, 2003). Similar to wild-type MEFs, $Topbp1^{B5/B5}$MEFs were able to activate DDR signaling responses when challenged with hydroxyurea and phleomycin as demonstrated by the induction of established damage-induced phosphorylation of CHK1, CHK2, RPA2 and KAP1 (Figure 2E). In addition, $Topbp1^{B5/B5}$ MEFs were able to recruit MDC1 to γH2AX-marked DSB foci when subjected to IR (Figure 2F) and showed no increased number of micronuclei, a known marker of defective DNA damage responses (Kwon et al., 2020), when compared to $Topbp1^{+/+}$ MEFs (Supplemental Figure 3A-B).

The BRCT-5 domain of TOPBP1 is known to interact with the DDR factors 53BP1(Bigot et al., 2019; Cescutti et al., 2010; Liu et al., 2017), MDC1(Wang et al., 2011) and BLM (Blackford et al., 2015) through phospho-protein binding modules. To investigate which, if any, of these interactions are disrupted upon mutating the eight BRCT5 residues, we ectopically expressed Flag-TOPBP1-WT or Flag-TOPBP1-B5 in HEK293T cells. We found that binding of Flag-TOPBP1-B5 to BLM and 53BP1 was impaired, as expected (Supplemental Figure 4A-B). Moreover, we noticed a 2-fold reduction in protein levels of Flag-TOPBP1-B5 compared to Flag-TOPBP1-WT, which could be explained by the loss of interaction with BLM (that was proposed to lead to protein stabilization (Balbo Pogliano et al., 2022; Wang et al., 2013), or by protein misfolding caused by the 8 eight K to E/D mutations. In addition, the reduction in protein levels was detected on MEFs (Supplemental Figure 5). In either case, the results presented here show that the TOPBP1-B5

mutant offers a unique model to separate roles of TOPBP1 in male meiosis from the canonical DDR functions of TOPBP1 in somatic cells.

$Topbp1^{B5/B5}$ spermatocytes display normal markers of canonical ATR signaling, chromosome synapsis, DNA repair, sex body formation, and DDR protein localization at the X and Y

TOPBP1 and ATR play multiple roles in spermatocytes during prophase I. Mice conditionally depleted for TOPBP1 (ElInati et al., 2017) or ATR (Royo et al., 2013; Widger et al., 2018) display severe defects in chromosome synapsis, DNA DSB repair, sex body formation and MSCI, as well as impaired recruitment of DDR factors to the XY (Pereira et al., 2020). Strikingly, analysis of $Topbp1^{B5/B5}$ spermatocytes via meiotic spreads revealed normal repair of DNA DSBs, with γH2AX staining grossly unchanged at pachynema, being confined only to the XY chromosomes and being excluded from the autosomes (Figure 3A-B). RAD51 localized only to the X and Y chromosomes during mid-pachytene (Figure 3C-D), indicating normal DSB repair at the autosomes. We were unable to detect chromosome synapsis abnormalities in $Topbp1^{B5/B5}$ spermatocytes, as $Topbp1^{B5/B5}$ mutant spermatocytes transit from zygotene into pachytene with normal patterns of HORMAD1 and HORMAD2 localization (Supplemental Figure 6A-B) and with SYCP1 overlapping with SYCP3 on chromosome cores from all autosomal chromosomes during pachynema (Figures 1L and 3E). Since ATR orthologs regulate crossing over in budding yeast (Subramanian and Hochwagen, 2014) and in *Drosophila melanogaster* (Carpenter, 1979), we also investigated the localization of factors involved in regulating DNA crossovers, including MLH1 and MLH3. In $Topbp1^{B5/B5}$ spermatocytes, while the number of MLH1 foci were significantly increased, the number of MLH3 foci did not differ significantly (Supplemental Figure 7A and 7B). Due to the lack of diplotene cells, and any other stage after pachynema, we were not able to test whether $Topbp1^{B5/B5}$ display defects in crossing over.

The sex body appeared normal in its shape and was normally formed in $Topbp1^{B5/B5}$ spermatocytes (Figures 3A and Supplemental Figures 8 and 9A), exhibiting only subtle defects/delays in the spreading of the γH2AX signal on the PAR and pericentromeric regions (Supplemental Figure 9B-G). Although the defect was subtle in its severity, it accounted for 56% of all γH2AX-stained mid-pachytene cells. Importantly, TOPBP1 was normally localized to X and Y chromosomes during prophase I (Supplemental Figure 10 and Figure 3F-H). Similarly, localization of the TOPBP1

interactors ATR, BRCA1, MDC1, and 53BP1 in *Topbp1*$^{B5/B5}$ spermatocytes spreads was also indistinguishable from that observed in *Topbp1*$^{+/+}$ spermatocytes (Figures 4A-F and Supplemental Figures 11). Markers of ATR signaling were also mostly normal, as measured by its canonical targets pMDC1 T4 (Supplemental Figure 6C-D), pCHK1 S345 (Supplemental Figure 6E-F), and pHORMAD2 (Supplemental Figure 6G-H). Notably, we did observe that phosphorylation of CHK1 on S317 was significantly decreased in *Topbp1*$^{B5/B5}$ when compared to *Topbp1*$^{+/+}$ spermatocytes (Figure 4G-H). However, since *Chk1* CKO spermatocytes complete prophase I and differentiate into spermatozoa, with only minor defects such a delay in the removal of γH2AX from autosomes (Abe et al., 2018), the observed defect in Chk1 S317 phosphorylation is unlikely to be the cause of the infertility observed in *Topbp1* B5 mutants. Overall, as summarized in Figure 4I, *Topbp1*$^{B5/B5}$ spermatocytes appear to progress normally through early stages of prophase I up until the end of pachynema as demonstrated by largely normal localization of markers for DNA repair, chromosome synapsis and ATR signaling. These findings are surprising because the lack of sex body formation, synapsis defects or unrepaired DSBs, which are the expected causes of the drastic loss of diplotene cells and the lack of spermatozoa, were not observed.

Defective phosphorylation and XY localization of the RNA:DNA helicase SETX in *Topbp1*$^{B5/B5}$ spermatocytes

With the exception of CHK1 phosphorylation at serine 317, the analysis of other canonical markers of ATR signaling on meiotic prophase I spreads did not reveal obvious defects in their distribution or intensity at the XY body (Figure 4G-H and Supplemental Figure 6C-H). Since altered CHK1 regulation is unlikely to be the cause of the drastic defect in meiotic progression observed in *Topbp1*$^{B5/B5}$ males, we investigated whether other branches of ATR signaling were altered in *Topbp1*$^{B5/B5}$ spermatocytes by performing unbiased quantitative phosphoproteomics based on TMT (Tandem Mass Tag (Thompson et al., 2003)) labeling of whole testes. Following a similar approach previously used by our group (Sims et al., 2022), we analyzed the phosphoproteome of *Topbp1*$^{B5/B5}$ and *Topbp1*$^{+/+}$ testes, and then compared the results to our previously reported dataset comparing the phosphoproteome of testes from mice treated with vehicle or the ATR inhibitor AZ20 (Sims et al., 2022) (Figure 5A). The resulting plot revealed that ATR-dependent signaling is not drastically impaired in *Topbp1*$^{B5/B5}$ testes, as opposed to the marked impairment of ATR signaling previously observed in testes of *Rad1* CKO mice (Sims et al., 2022). This finding is in

agreement with the results from meiotic spreads of *Topbp1*$^{B5/B5}$ showing no detectable defects in canonical markers of ATR signaling described above. Nonetheless, our phosphoproteomic analysis did reveal phosphorylation sites mildly disrupted in *Topbp1*$^{B5/B5}$ testes compared to *Topbp1*$^{+/+}$ testes. In particular, we noticed that several phosphorylation sites in the RNA:DNA helicase, Senataxin (SETX) (Cohen et al., 2018), including a phosphorylation in the preferred motif for ATR phosphorylation (S/T-Q), were down-regulated in *Topbp1*$^{B5/B5}$ mice (Figure 5B). Interestingly, SETX was previously associated with meiotic ATR functions and found to be indispensable for MSCI (Becherel et al., 2013; Yeo et al., 2015). Moreover, we recently reported that mice treated with the ATR inhibitor AZ20 or lacking *Rad1* display reduced phosphorylation of SETX at S/T-Q site and SETX mislocalization during pachynema (Sims et al., 2022). Based on our findings, we propose that TOPBP1 regulates SETX distribution and/or function during meiosis, and that defects in meiotic progression and fertility observed in *Topbp1*$^{B5/B5}$ mice might be associated with SETX dysfunction. Consistent with this possibility, we found that pachytene spermatocytes from *Topbp1*$^{B5/B5}$ display significantly decreased spreading of SETX to XY chromatin loops while still displayed SETX at the unsynapsed axes of the X and Y chromosomes (Figures 5C-F). Overall, these findings reveal that *Topbp1*$^{B5/B5}$ spermatocytes display largely normal progression through mid-pachynema, as demonstrated by normal distribution of a range of markers of meiotic progression, including canonical markers of ATR signaling. However, in-depth phosphoproteomic and imaging analyses identify specific defects in the regulation of SETX, a target of ATR signaling during prophase I (Pereira et al., 2022; Sims et al., 2022) and a key factor required for MSCI (Becherel et al., 2013; Yeo et al., 2015).

Topbp1$^{B5/B5}$ spermatocytes initiate MSCI but fail to promote full XY silencing

During mid-pachynema, spermatocytes that fail to properly silence the X and Y chromosomes arrest and trigger apoptosis-induced cell death (Abe et al., 2020; Ichijima et al., 2012; Turner, 2015, 2007). In mice, the MSCI process initiates in leptonema (Lau et al., 2020), and during early pachynema key events occur at the XY chromosomes, such as exclusion of RNA polymerase 2 (RNA Pol2), recruitment of DDR proteins and chromatin remodelers and establishment of heterochromatin marks (Abe et al., 2020; Khalil et al., 2004) to maintain the active silencing of the X and Y chromosomes (Abe et al., 2022). This process leads to the formation of a membrane-less phase separated structure termed the sex body (Alavattam et al., 2022; Xu and Qiao, 2021).

Spermatocytes from *Topbp1*$^{B5/B5}$ males formed a sex body of grossly normal appearance (Supplemental Figure 8), with undisrupted patterns of the sex body markers CHD4, SUMO, and USP7 (Supplemental Figure 12). *Topbp1*$^{B5/B5}$ pachytene spermatocytes also display normal patterns of a range of chromatin marks, including H3K9ac, H3K9me3, H3K27ac, H3K36me3, H3K4me3, H4K16ac, H4ac, H2AK116ub, H3K4me1, as well as proper exclusion of RNA Pol2 from the sex body (Supplemental Figures 13-17). Collectively the evidence presented herein shows that *Topbp1*$^{B5/B5}$ mutants are able to form grossly normal XY bodies, with proper localization of over 28 markers, the severe loss of diplotene cells and the reduction of SETX at the chromatin loops of the X and Y lead us to speculate that *Topbp1*$^{B5/B5}$ spermatocytes may still have a defective MSCI. To investigate potential MSCI defects, we employed single cell RNA sequencing (sc-RNA-seq) in germ cells (Figure 6A) using a similar approach recently used to follow spermatogenesis progression and to evaluate MSCI in mammals (Grive et al., 2019; Jung et al., 2019; Lau et al., 2020). Using the 10X platform we performed sc-RNA-seq on a germ cell-enriched population of cells extracted from adult *Topbp1*$^{+/+}$ and *Topbp1*$^{B5/B5}$ testes (Figure 6A). The data were analyzed as previously described (Grive et al., 2019; Lau et al., 2020) using signature genes as markers of different stages in spermatogenesis such as, *Sal4* and *Dmrt1* for spermatogonia, *Dazl* for early spermatocytes, *Id4*, *Sycp3* and *Shcbp1l* for late spermatocytes, *Acrv1* for round spermatids, and *Oaz3* and *Prm2* for elongated spermatids (Supplemental Figures 18 and 19). *Col1a2*, *Acta2*, *Vcam1*, *Lnsl3*, *laptm5*, *Hbb-bt*, *Ptgds* and *Wt1* were used as markers of somatic cells (Supplemental Figure 20). Analysis of the testicular transcriptome of *Topbp1*$^{+/+}$ males revealed 47 sub-clusters of cells covering spermatogonia, spermatocytes, spermatids, and somatic cells (Figure 6B-D and Supplemental Figures 21-22). In sharp contrast, analysis of *Topbp1*$^{B5/B5}$ germ cell population revealed only somatic, spermatogonia and the initial populations of spermatocytes (Figure 6D). This result corroborates the H&E-stained testes histological sections (Figure 1I) and meiotic spreads (Figure 1L). Importantly, Pearson correlation values from all RNA reads between cell groups separated by cluster and genotype, demonstrated the similarity of spermatocytes from *Topbp1*$^{+/+}$ and *Topbp1*$^{B5/B5}$ (Supplemental Figure 23). As shown in Figure 6E, we were able to monitor the dynamics of X chromosome silencing in the early-stage spermatocytes and compare the results between RNA from *Topbp1*$^{+/+}$ and *Topbp1*$^{B5/B5}$ males. Strikingly, *Topbp1*$^{B5/B5}$ early-stage spermatocytes could initiate MSCI and promote robust, albeit incomplete, X chromosome silencing. Both X and Y chromosomes showed increased gene expression levels in the last

spermatocyte stage captured in *Topbp1*$^{B5/B5}$ males when compared to RNA from wild type males (Figure 6E and Supplemental Figure 24). Moreover, although certain X-genes from *Topbp1*$^{B5/B5}$ pachytene cells consistently demonstrated defects in silencing by being expressed in numerous cells, other genes were only expressed in a small number of cells. This highlights the non-uniformity of the MSCI defect in all pachytene cells (Supplemental Figure 24). Notably, while we detected only a minor elevation in the levels of X-linked gene expression in *Topbp1*$^{B5/B5}$ spermatogonia when compared to *Topbp1*$^{+/+}$, the expression of X-linked genes at spermatocyte 3 stage was drastically higher in *Topbp1*$^{B5/B5}$ males when compared to *Topbp1*$^{+/+}$ males. To improve the accuracy of the downstream analysis, the expression levels of X-linked genes were normalized by their respective expression level at the pre-leptotene stage.

MSCI is a dynamic process that involves the accumulation of DDR factors at the X and Y chromosomes as cells enter pachynema (Abe et al., 2022, 2020) as well as the inactivation of specific X and Y genes that lead to cell death if expressed at this stage (the so called "killer genes") (Royo et al., 2010; Vernet et al., 2016). Similar to previous reports based on mutants or treatments that impaired MSCI (Abe et al., 2022; ElInati et al., 2017; Hirota et al., 2018; Modzelewski et al., 2012; Pereira et al., 2022; Royo et al., 2013; Widger et al., 2018), transcriptomics profiles from *Topbp1*$^{B5/B5}$ testicular cells showed an increased number of stage 3 spermatocytes (SP3 - pachytene) expressing the spermatocyte-toxic genes *Zfy1* and *Zfy2* compared to *Topbp1*$^{+/+}$ (Supplemental Figures 25-26). Other genes typically used to illustrate MSCI defects, such as *Kdm6a*, *lamp2*, *Zfx*, *Uba1y* and *Rhox13* were also expressed in a higher number of SP3 cells in *Topbp1*$^{B5/B5}$ (Supplemental Figures 25-26). In the case of *Scml2*, *Topbp1*$^{B5/B5}$ cells not only displayed an increased number of SP3 (pachytene) cells expressing it but also displayed an increase in expression levels in these cells compared to *Topbp1*$^{+/+}$ testes (Supplemental Figures 25-26). In summary, various Y and X genes that had previously been shown to be expressed in other MSCI-defective mutants were found de-repressed in *Topbp1*$^{B5/B5}$ spermatocytes.

Detailed analysis of the scRNA-seq data for the X-linked genes monitored during the early spermatocyte stages revealed important differences in the silencing dynamics of these X genes between *Topbp1*$^{B5/B5}$ and *Topbp1*$^{+/+}$ spermatocytes. 233 out of the roughly 700 genes present on the X chromosome had reads detected from pre-leptotene to spermatocyte 3 clusters for both

Topbp1$^{+/+}$ and *Topbp1*$^{B5/B5}$ cells, and therefore were used during the downstream analysis. As shown in Figure 7A, we clustered the X-linked genes into 3 distinct categories based on the change of RNA level between the stages: reduced, unaltered, or increased silencing (Figures 7A). SP1 (spermatocyte 1) was defined as leptotene using the gene marker *Gm960* (Chen et al., 2018) (Supplemental Figure 27), and SP2 (spermatocyte 2) as zygotene due to its profile of low expression of *Gm960* and high expression of *Dazl*. SP3 (spermatocyte 3) was defined as pachytene due to its lower expression of *Dazl* and increased expression of *Id4* and *Shcbp1l*. When comparing the distribution of genes in these clusters between *Topbp1*$^{B5/B5}$ and *Topbp1*$^{+/+}$ spermatocytes (RNA level normalized to pre-leptotene stage) (Figure 7B), we observed no major differences in the pre-leptotene to spermatocyte 1 (PL to SP1) and in the spermatocyte 1 to spermatocyte 2 (SP1 to SP2) transitions. In contrast, when comparing the spermatocyte 2 to spermatocyte 3 (SP2 to SP3) transition between *Topbp1*$^{B5/B5}$ and *Topbp1*$^{+/+}$ spermatocytes we noticed a major difference in the distribution of the clusters, with 74 genes in *Topbp1*$^{B5/B5}$ versus 4 in *Topbp1*$^{+/+}$ exhibiting reduced silencing (Figure 7B). Moreover, while 134 genes showed unaltered silencing, and only 24 increased silencing in *Topbp1*$^{B5/B5}$ spermatocytes during the SP2 to SP3 transition, 43 genes showed unaltered silencing and 185 increased silencing in *Topbp1*$^{+/+}$ (Figure 7B). *Xiap*, *Zc3h12b* and *Cetn2* are examples of X-linked genes displaying altered silencing behaviors in *Topbp1*$^{B5/B5}$ spermatocytes (Figure 7C). The difference of expression between *Topbp1*$^{+/+}$and *Topbp1*$^{B5/B5}$ was markedly higher in the SP2 to SP3 transition compared to the other transitions (Figure 7D-E) and was used to further split genes into 3 categories based on the severity of the silencing defect in *Topbp1*$^{B5/B5}$: no defect (13 genes), mild (45 genes) or strong defect (170 genes) (Figure 7F). Notably, the severity of the silencing defect of a gene had some correlation with its RNA level in the pre-leptotene stage, with highly expressed genes having a higher tendency to have a more severe silencing defect (Figure 7G and Supplemental Figure 28). Taken together, these data characterize the specific silencing defect in *Topbp1*$^{B5/B5}$ spermatocytes and point to a specific role for TOPBP1 in ensuring proper silencing dynamics after an initial wave of MSCI, likely through later waves of silencing reinforcement. Our data is consistent with the notion that silencing of the X and Y chromosomes is a dynamic process that needs active and continuous engagement by the ATR-TOPBP1 signaling axis. Since the majority of the mouse models of male infertility accumulate pleiotropic defects, with disrupted MSCI and absence of sex body, the *Topbp1*$^{B5/B5}$

mouse reported here provides a unique model of DDR impairment in which MSCI can be uncoupled from sex body formation (Figure 8).

Discussion

In male meiosis I, DDR factors such as ATR, TOPBP1, BRCA1, and the 9-1-1 complex play crucial roles in DNA repair, chromosome synapsis, recombination, sex body formation, and silencing (Broering et al., 2014; ElInati et al., 2017; Pacheco et al., 2018; Pereira et al., 2022; Royo et al., 2013; Turner et al., 2004; Widger et al., 2018). Conditional depletion of these factors results in pleiotropic phenotypes from compound effects in multiple processes, with cells ultimately undergoing apoptotic-induced cell death during the pachytene checkpoint. Here, we report a mutant mouse model capable of deconvoluting TOPBP1's roles during meiosis I in males, separating its role in silencing from its roles in DNA repair, synapsis and checkpoint signaling (Figure 8). While *Topbp1*$^{B5/B5}$ spermatocytes initiate XY silencing with similar dynamics as observed in *Topbp1*$^{+/+}$ these cells fail to complete silencing at the final steps of MSCI. Of note, *Topbp1*$^{B5/B5}$ cells displayed slightly higher expression of X-linked genes than *Topbp1*$^{+/+}$ cells in the earlier spermatogenic stages (from spermatogonia 1 to spermatocyte 3). Furthermore, not all X-linked genes in *Topbp1*$^{B5/B5}$ spermatocytes were silenced; instead, some genes were only partially silenced while others exhibited increased expression after initial silencing. This is consistent with previous reports using mouse mutants with more severe MSCI defects, such as *Ago4*$^{-/-}$ and *Topbp1 CKO*, in which not all X-linked genes exhibited altered levels of expression (ElInati et al., 2017; Modzelewski et al., 2012). Interestingly, a sex body is formed that is morphologically indistinguishable from the sex body in wild-type animals. Several heterochromatin markers, as well as multiple canonical markers of sex body formation localize properly in the sex body of *Topbp1*$^{B5/B5}$ mice. Overall, these findings suggest a non-canonical role for the ATR-TOPBP1 signaling axis in ensuring proper XY silencing dynamics during pachynema. This is the first DDR mutant that separates XY silencing from sex body formation, and that separates TOPBP1's role in spermatogenesis from its roles in organismal viability.

The *B5* allele reported here, which carries eight lysine to glutamic/aspartic acid substitutions in BRCT domain 5, is the first mutation shown to impair the meiotic silencing function of TOPBP1 in spermatocytes without severely disturbing TOPBP1's role in synapsis and sex body formation. Consistent with this being a separation of function mutant, *Topbp1*$^{B5/B5}$ males are viable and grossly normal, while completely sterile, whereas *Topbp1* null, or AAD mutated, mice are

embryonic lethal (Jeon et al., 2011; Zhou et al., 2013). Moreover, depletion of TOPBP1 in mammalian cell lines triggers a robust G2/M arrest followed by cell senescence and loss of viability (Jeon et al., 2011) *Topbp1*$^{B5/B5}$ MEFs do not display issues with cell proliferation or DDR defects. Based on these observations, and the finding of a silencing defect in *Topbp1*$^{B5/B5}$ spermatocytes, it is likely that the role of TOPBP1 in silencing documented here could be specifically relevant in the context of male meiosis. It is important to note that other mutants previously reported to have XY silencing defects during meiotic prophase I, such as *Ago4* null and *Dicer* CKO, do not result in complete loss of sperm production, but a sub-fertility phenotype (Greenlee et al., 2012; Modzelewski et al., 2012). Therefore, we speculate that the specific type of silencing defect in *Topbp1*$^{B5/B5}$ spermatocytes is particularly toxic, similar to other mutations in the DDR pathway that result in MSCI defects, which would explain the highly penetrant defect in sperm production.

The model that distinct TOPBP1 interactions mediate distinct ATR signaling pathways offers a potential explanation for why *Topbp1*$^{B5/B5}$ have specific defects in silencing without noted effects in other key processes regulated by ATR, such as synapsis. In addition to binding and activating ATR through its AAD domain (Mordes et al., 2008; Pereira et al., 2020), TOPBP1 can bind to several proteins through its BRCT domains (Yamane et al., 2002) and act as a scaffolding protein to bring substrates in close proximity to ATR, thus facilitating the propagation of specific ATR signaling pathways. Experiments using ectopic expression of Flag-tagged TOPBP1 in HEK293T cells revealed that the set of mutations in *B5* disrupt the ability of TOPBP1 to interact with 53BP1 and BLM, as expected from previous reports (Bigot et al., 2019; Blackford et al., 2015; Cescutti et al., 2010; Liu et al., 2017; Wang et al., 2013). However, it is unclear if the same interactions are also disrupted in spermatocytes, or whether additional TOPBP1 interactions mediated by its BRCT5 specifically during meiotic prophase I are also disrupted. Apart from disrupting protein interactions, it is also possible that the observed changes in TOPBP1 protein stability in the *Topbp1 B5* mutant can contribute to impairing its roles in silencing. Such change in protein stability is consistent with a previous report showing that the TOPBP1-BLM interaction contributes to protein stabilization (Balbo Pogliano et al., 2022; Wang et al., 2013). Further work will be necessary to determine if the phenotypes observed in *Topbp1*$^{B5/B5}$ spermatocytes are caused specifically by disruption of specific protein interactions, or by a combination of disrupted interactions and

reduced protein abundance. It is worth mentioning that the *Topbp1*$^{B5/B5}$ phenotype is distinct from the *Topbp1* CKO despite the reduction in protein abundance.

Our finding that SETX localization to chromatin loops of the XY is impacted in *Topbp1*$^{B5/B5}$ pachytene spermatocytes, together with our previous report that SETX undergoes ATR-dependent phospho-regulation in spermatocytes (Sims et al., 2022), suggest that an ATR-TOPBP1-SETX signaling axis is important for the silencing reinforcement in late MSCI. Genetic data support that impairment of this specific signaling axis would impact silencing without impacting synapsis. For example, *Topbp1* CKO, *Rad1* CKO, and *Atr* CKO spermatocytes display strong synapsis defect and defective entry in pachynema (ElInati et al., 2017; Widger et al., 2018), whereas *Setx* null spermatocytes complete autosomal synapsis, while still displaying MSCI defects. On the other hand, is it likely that ATR signaling is controlling a specific aspect of SETX function since *Topbp1*$^{B5/B5}$ spermatocytes do not share all defects observed in *Setx* null spermatocytes, as noted by the localization of γH2AX, sumoylation events, ubH2A and ATR at chromatin loops, which are defective in *Setx* null spermatocytes but normal in *Topbp1*$^{B5/B5}$ spermatocytes. Moreover, *Topbp1*$^{B5/B5}$ pachytene spermatocytes, but not *Setx* null spermatocytes, are able to reach the stage of crossover designation with MLH1 positive cells. Taken together, these observations suggest that *Topbp1*$^{B5/B5}$ pachytene spermatocytes progress further in pachynema when compared to *Setx* null spermatocytes and are consistent with a model in which a ATR-TOPBP1 control only specific(s) mode of SETX regulation (Pereira et al., 2022; Sims et al., 2022).

The model involving SETX as a potential factor by which ATR controls silencing late in MSCI opens exciting directions to explore the interface of ATR-TOPBP1 with RNA processing. Given the established role for SETX in the resolution of R-loops (Bennett and La Spada, 2018), it is tempting to speculate that silencing defects in *Topbp1*$^{B5/B5}$ mutant may be related to aberrant accumulation of RNA-DNA hybrids that may affect removal of nascent mRNAs that is necessary for imposing silencing. This hypothesis assumes that the silencing of X and Y genes is a dynamic process involving ongoing mechanisms of exclusion of RNA polymerase II and nascent RNA, as proposed recently (Abe et al., 2022; Sims et al., 2022). Moreover, the model predicts that SETX function is specifically affected in the sex body, which is consistent with the observed defect in SETX localization. In support of this model, R-loops affect chromatin architecture at promoters

and interfere with the recruitment of transcription factors and chromatin remodelers, as observed in regions harboring CpG islands where R-loops prevent the action of DNA methyltransferases, thus preventing silencing (Santos-Pereira and Aguilera, 2015). Notably, highly transcribed genes, which tend to accumulate more R-loops (Marnef and Legube, 2020), displayed increased silencing defects in the *Topbp1*$^{B5/B5}$ mutant.

While we have provided strong evidence to suggest a defect in later stages of MSCI as the cause of the cell death observed in *Topbp1*$^{B5/B5}$ spermatocytes, we cannot exclude the potential contribution of other defects, beyond silencing, to the loss of diplotene cells. The increased number of MLH1 foci suggested an altered recombination pattern, possibly impairing the ratios of class I and class II crossovers. The BRCT 5 domain of TOPBP1 interacts with the BLM helicase (Balbo Pogliano et al., 2022; Blackford et al., 2015), which has been found to play a role in meiotic recombination in yeast and mice (Holloway et al., 2010; Rockmill et al., 2003). *Blm* CKO mice display severe defects in prophase I progression in spermatocytes, including, incorrect pairing and synapsis of homologs, and defective processing of recombination intermediates, leading to increased chiasmata (Holloway et al., 2010). These observations raise the possibility that impaired meiotic progression and cell death in *Topbp1*$^{B5/B5}$ spermatocytes is a combination of defects in MSCI and recombination. *Topbp1*$^{B5/B5}$ spermatocytes do not progress beyond pachytene hence we were not able to visualize chiasmata and directly infer whether or not *Topbp1*$^{B5/B5}$ is defective in crossing over. Of note, MLH1 and MLH3 are known to form a heterodimer in the context of meiotic recombination (Lipkin et al., 2000; Svetlanov et al., 2008). While our data show increased MLH1 foci counts in *Topbp1*$^{B5/B5}$, MLH3 foci counts were not different from *Topbp1*$^{+/+}$, thus, we cannot exclude the possibility that the imbalance between MLH1 and MLH3 might affect the loss of diplotene cells in *Topbp1*$^{B5/B5}$ through processes not related to crossing over. Importantly, while MLH3 works exclusively as a heterodimer with MLH1, MLH1 can function in a heterodimeric complex with other MutL homologs (Nakagawa et al., 1999).

Our findings showing that TOPBP1 plays a specific role in silencing reinforcement after the first wave of MSCI are consistent with the recently proposed notion that the establishment and maintenance of MSCI is a dynamic process (Abe et al., 2022; Sims et al., 2022). Also consistent with this notion is our recent finding showing that ATR signaling is itself also highly dynamic and

constantly being cycled (Sims et al., 2022). For example, using mice treated with the ATR inhibitor (ATRi) AZ20 for four hours, we found that such a short treatment is already sufficient to cause a complete loss of γH2AX, pMDC1 and SETX localization from the XY chromosomes (Abe et al., 2022; Sims et al., 2022). Furthermore, germ cells subjected to ATRi for 24 hours showed complete recovery of γH2AX only three hours after release from ATRi treatment (Abe et al., 2022). We propose that TOPBP1 acts on this phospho-cycle to ensure proper silencing reinforcement and maintenance, potentially by counteracting the engagement of anti-silencing factors that dynamically enter the sex body and need to be actively antagonized at the XY. Future work involving the characterization of possible unknown interactors of the BRCT domain 5 of TOPBP1, as well as functional dissection of ATR targets in MSCI, is essential to understand how TOPBP1 modulates the silencing machinery and shapes silencing dynamics. Interestingly, while we propose that the lack of silencing maintenance is the major defect causing the pachytene cell death in *Topbp1*$^{B5/B5}$ spermatocytes, we cannot exclude the possibility that the expression of XY-linked genes could represent a regulated response to meiotic defects more than a mere consequence of a defective MSCI. If this latter hypothesis is true, the cell death caused by defects in the XY chromosomes would be independent of MSCI. Notably, this hypothesis could not have been conceptualized prior to this work given that the majority of prophase I mutants characterized to this date are unable to reach the stage where MSCI is properly established. Thus, the *Topbp1*$^{B5/B5}$ is a unique model allowing future studies that may uncouple MSCI from XY-triggered cell death during pachynema.

In summary, our study presents a unique model for investigating the role of DDR factors in XY silencing. By allowing the uncoupling of MSCI progression from sex body formation, the *Topbp1*$^{B5/B5}$ mutant enables the study of MSCI dynamics during key stages late in pachynema. Notably, the inability of *Topbp1*$^{B5/B5}$ to sustain or reinforce silencing opens the possibility of uncovering new insights into the MSCI-dependent pachytene checkpoint.

Materials and methods

Key resource table

Reagent type	Designation	Source or Reference	Identifiers	Additional information
Primer	p3xflag-TOPBP1-Flag-N-terminal-F	IDT	PCR primer	attcatcgatagatctgata ATGTCCAGAAAT GACAAAGA
Primer	p3xflag-TOPBP1-Flag-N-terminal-R	IDT	PCR primer	tagagtcgactggtaccgat ttagTGTACTCTAG GTCGTT
Primer	hTopbp1_K1317A_R	IDT	Site-directed mutagenesis	tgccactgaggctaaatac gcctcgtttcgaagtggatg t
Primer	hTopbp1_K1317A_F	IDT	Site-directed mutagenesis	acatccacttcgaaacgag gcgtatttagcctcagtggc a
Primer	hTopbp1_K155A_F	IDT	Site-directed mutagenesis	caggtttgcagcaactaaat atgctttgctaccaacttctc ctgca
Primer	hTopbp1_K155A_R	IDT	Site-directed mutagenesis	tgcaggagaagttggtagc aaagcatatttagttgctgca aacctg
Primer	hTopbp1_K250A_R	IDT	Site-directed mutagenesis	tctcttggcacactcatacg cctgacctttggttcttgc
Primer	hTopbp1_K250A_F	IDT	Site-directed mutagenesis	gcaagaaccaaaaggtca ggcgtatgagtgtgccaag aga
Primer	musTopbp1_BRCT5-Fwd genotyping	IDT	PCR primer	tgcatttccattaaccaacct c
Primer	musTopbp1_BRCT5 Rev genotyping	IDT	PCR primer	ggtagagttcaaatgtgtgt catg
Antibody	phospho H2A.X (Ser139)	Millipore	Cat# 05-636;RRID:AB_309864	IF (meiotic spreads) 1:50000 IF 1:2000

Antibody	SCP3 antibody	Abcam	Cat# ab97672;RRID: AB_10678841	IF (meiotic spreads) 1:1000
Antibody	SYCP3	(Lenzi et al., 2005)	Custom	IF (meiotic spreads) 1:10000
Antibody	SCP1	Abcam	ab15090	IF (meiotic spreads) 1:1000
Antibody	Rad51	Millipore	PC130	IF (meiotic spreads) 1:1000
Antibody	ATR	Cell signaling	2790	IF (meiotic spreads) 1:1000
Antibody	TOPBP1	(Danielsen et al., 2009)	Custom	IF (meiotic spreads) 1: 500 Western blot 1:1000
Antibody	phospho-Chk1 (ser317)	Cell Signaling	12302	IF (meiotic spreads) 1: 100 Western blot 1:1000
Antibody	H1T	A gift from Dr. Mary Ann Handel (Inselman et al., 2003)	Custom	IF (meiotic spreads) 1: 500
Antibody	HORMAD2	(Wojtasz et al., 2012)	Custom	IF (meiotic spreads) 1: 500
Antibody	HORMAD1	(Wojtasz et al., 2012)	Custom	IF (meiotic spreads) 1: 500
Antibody	phospho HORMAD2 (S271)	(Wojtasz et al., 2009)	Custom	IF (meiotic spreads) 1: 500
Antibody	GAPDH	Thermo Fisher Scientific	AM4300	Western blot 1:5000
Antibody	β-Actin	Cell Signaling	4967	Western blot 1:5000
Antibody	phospho MDC1 (T4)	Abcam	Ab35967	IF (meiotic spreads) 1: 500

Antibody	SETX	Abcam	Ab220827	IF (meiotic spreads) 1: 100
Antibody	SETX	Novus Biologicals	NBP1-94712SS	Western blot 1:1000
Antibody	MLH1	BD Biosciences	550838	IF (meiotic spreads) 1: 200
Antibody	MLH3	A gift from Dr. Paula Cohen (Holloway et al., 2014)	Custom	IF (meiotic spreads) 1: 200
Antibody	CHK1	Santa Cruz	sc-8408	Western blot 1:1000
Antibody	CHK2	Millipore	05-649 (clone7)	Western blot 1:1000
Antibody	phospho CHK1 (S345)	Cell Signaling	2341	IF (meiotic spreads) 1: 200 Western blot 1:1000
Antibody	phospho RPA (S4/S8)	Bethyl	A300-245A,	Western blot 1:1000
Antibody	RPA (made against full length RPA2 expressed and purified in *E. Coli* and injected to rabbit)	N/A	Custom	Western blot 1:1000
Antibody	KAP1	Bethyl	a700-014-T	Western blot 1:1000
Antibody	phospho KAP1 (S824)	Bethyl	A300-767A-T	Western blot 1:1000
Antibody	53BP1	Cell signaling	4937	Western blot 1:1000
Antibody	53BP1	Novus Biologicals	NB100-304	IF (meiotic spreads) 1: 200
Antibody	BLM	Abcam	ab2179	Western blot 1:500
Antibody	Rad9	Bethyl	A300-890A-T	Western blot 1:1000
Antibody	BRCA1	(Kakarougkas et al.,	Custom	IF (meiotic spreads) 1: 200

		2013)		
Antibody	BRCA1	Proteintech	22362-1-AP	Western blot 1:1000
Antibody	MDC1	(Modzelewski et al., 2015)	Custom	IF (meiotic spreads) 1: 200 IF 1: 200
Antibody	RNA pol 2	Millipore	05-623	IF (meiotic spreads) 1: 2000
Antibody	phospho RNA pol 2 (Ser2)	Millipore	04-1571	IF (meiotic spreads) 1: 400
Antibody	phospho RNA pol 2 (Ser5)	Millipore	04-1572	IF (meiotic spreads) 1: 400
Antibody	H3K9ac	Abclonal	A7255	IF (meiotic spreads) 1: 200
Antibody	H3K9me3	Active Motif	39766	IF (meiotic spreads) 1: 200
Antibody	H3K4me1	Abclonal	A2355	IF (meiotic spreads) 1: 200
Antibody	CHD4	Abclonal	A10557	IF (meiotic spreads) 1: 200
Antibody	Sumo_2/3	Proteintech	G67154-1-1g	IF (meiotic spreads) 1: 200
Antibody	USP7	Proteintech	66514-1-Ig	IF (meiotic spreads) 1: 200
Antibody	H3K27ac	Active Motif	39134	IF (meiotic spreads) 1: 200
Antibody	H3K36ac	Active Motif	61102	IF (meiotic spreads) 1: 200
Antibody	H3K4me3	Active Motif	39160	IF (meiotic spreads) 1: 200
Antibody	H4K16ac	Abclonal	A5280	IF (meiotic spreads) 1: 200
Antibody	H4c	Millipore	06-598	IF (meiotic spreads)

				1: 200
Antibody	H2AK199ub	Abcam	Ab193203	IF (meiotic spreads) 1: 200
Antibody	Goat anti-rabbit IgG (H + L) highly cross-adsorbed secondary antibody, Alexa Fluor 488	Thermo Fisher Scientific	A-11034	IF (meiotic spreads) 1: 1000
Antibody	Goat anti-mouse IgG (H + L) antibody, Alexa Fluor 488 conjugated	Thermo Fisher Scientific	A-11017	IF (meiotic spreads) 1: 1000
Antibody	Goat anti-rabbit IgG (H + L) antibody, Alexa Fluor 594 conjugated	Thermo Fisher Scientific	A-11012	IF (meiotic spreads) 1: 1000
Antibody	Goat anti-mouse IgG (H + L) highly cross-adsorbed secondary antibody, Alexa Fluor Plus 594	Thermo Fisher Scientific	A32742	IF (meiotic spreads) 1: 1000
Antibody	Goat anti-guinea pig IgG (H + L) highly cross-adsorbed secondary antibody, Alexa Fluor 647	Thermo Fisher Scientific	A-21450	IF (meiotic spreads) 1: 1000
Commercial assay or kit	ApopTag Plus Peroxidase In Situ Apoptosis Kit	Millipore	S7101	N/A
Software, algorithm	GraphPad Prism 9	GraphPad Prism	RRID:SCR_002798	N/A
Software	Cellranger v7.0.0	10X Genomics	https://support.10xgenomics.com/single-cell-gene-expression/software/download	N/A

			s/3.1	
Software	R v4.2.1	R Foundation	RRID:SCR_001905	N/A
Software	Seurat v4.3.0	(Hao et al., 2021)	RRID:SCR_007322	N/A
Software	sva v3.44.0	(Leek et al., n.d.)	RRID:SCR_012836	N/A
Software	SingleR v1.10.0	(Aran et al., 2019)	RRID:SCR_023120	N/A
Software	Reshape2 v1.4.4	(Wickham, 2007)	RRID:SCR_022679	N/A
Software	biomaRt v2.52.0	(Durinck et al., 2009)	RRID:SCR_019214	N/A
Software	ggpubr v0.5.0	(Kassambara, 2019)	RRID:SCR_021139	N/A
Software	Tidyverse v1.3.2	(Wickham et al., 2019)	RRID:SCR_019186	N/A
Software	ggnewscale v0.4.8	Campitelli	https://eliocamp.github.io/ggnewscale/index.html	N/A

Software	Harmony v0.1.1	(Korsunsky et al., 2019)	RRID:SCR_022206	N/A
Software	Org.Mm.eg.db v3.15.0	(Carlson et al., n.d.)	RRID:SCR_023488	N/A
Software	Corrplot v0.92	(Wei and Simko, 2017)	RRID:SCR_023081	N/A
Software	SeuratWrappers v0.3.1	Satija Lab	RRID:SCR_022555	N/A
Software	gghalves v0.1.4	Tiedemann	https://github.com/erocoar/gghalves	N/A

Resource availability

Lead contact

Further information and requests for resources and data should be directed to and will be fulfilled by the lead contact, Marcus Smolka (email: mbs266@cornell.edu).

Materials availability

This study generated a unique antibody, RPA.

Mice, genotyping and treatment of mice with IR

All mice used in this work were handled following federal and institutional guidelines under a protocol approved by the Institutional Animal Care and Use Committee (IACUC) at Cornell University. CRISPR/Cas9 editing was used to engender the *Topbp1B5* allele and performed by the Cornell Mouse Modification core facility. To this end, the online tools CRISPR gold and

ChopChop were used to generate high quality (guide score >9) CRISPR guide RNAs targeting the intronic sequences neighboring the genomic sequence of *Mus musculus topbp1* exon 13. The CRISPR crRNAs (purchased from IDT) harboring the sequences ccaactcaggtcggccgctcttg and cctcgattagtcctcaaggcgag (PAM sites are underlined), both targeting the reverse strand, the repair template (below), and CAS9 RNA were injected on embryos from super ovulated, plugged C57BL/6J female mice crossed to C57BL/6J stud males. 2-cell stage embryos were then implanted on pseudo pregnant females and pups were genotyped after one week old.

Repair template:

acagcagggcttctctgtgtaaccctctctccgtagaccagtttggccttgatcgaactcaggtcggccgctcttgcctctagagtcctgggat
taaaggcgtgcactgccaccacccagagtatgtttctctgacattaaccatgctattattttttaaaatgagctaattgtgtgttcatttgctttattt
ccatgtaaaattttagTGTTCAAGAATTCTTTGTTGACGAAGCCAATGCAGAGGAAGGCATGCT
CGCCAGCACACATCTTATAGTGGAGGAACCGACTGGTTCCGAATACGAAGCTGCAG
AGGAATGGAGTTTGCCGGCAGTTAACATTTCATGGCTCTTAGAAACTGCGGAAATCG
GGGAGGAAGCAGATGAAAACCATTTTCTGGTTGACAACGCACCTAAACAAGgttagaagt
ccttgtttttttttatgtattttacaacttgatggtttctgaaatagggatgttccagtacttgctttaaaacatttgtatgaccctaacctcagtcagtg
gtgcttacttcagaacccctgagtgaaacacggaaagcagatcaatgaagaagcgcatcagggtcaacggtcgattagtcctcaaggcga
gtgacgagaaggtgacccccga atggctgttagaagcagtttttata (purchased from IDT as a G-block)

Intronic sequence is shown in lower case, exon 13 sequence is shown in capital letters; underline represents the mutated residues, pink represents the mutated PAM residues, in orange is shown the guide RNA sequences and in red, the targeted amino acid sequences. Of note, although this repair template encodes for 11 amino acid changes, only 8 were successfully inserted into the mouse topbp1 exon 13 locus. For mice genotyping, the following primers were used 5'-tgcatttccattaaccaacctc-3' and 5'- ggtagagttcaaatgtgtgtcatg-3' (also shown at key resources table). For irradiation, *Topbp1*$^{+/+}$ and *Topbp1*$^{B5/B5}$ mice were placed in a 137 Cesium-sealed source irradiator (J.L. Shepherd and Associates) with a rotating turntable and irradiated with 7 Gy IR.

MEFs and cell survival assays

MEFs were prepared from E13.5 mouse embryos as previously described (Balmus et al., 2012). Briefly, embryos were dissected and mechanically disrupted using pipette aspiration until homogenous. Cells were allowed to settle, and the supernatant was transferred into Dulbecco's modified medium supplemented with 10% fetal bovine serum, 1% penicillin/streptomycin and 1%

nonessential amino acids. Following four days of growth, cells were then immortalized by transduction with a large-T antigen lentivirus. Subsequently, cells were selected with 10 µg/mL puromycin.

For colony survival assays, 500 cells were seeded per 10 cm dish, allowed to adhere for 24h and treated with Phleomycin or Hydroxyurea for 24h (drug concentrations are displayed on figure 2A-D and Supplemental Figure 2). In the following day, cells were released and let to form colonies for 10-15 days. Cells were then washed once with PBS, fixed in 100% methanol for 1h, stained with 0.1% crystal violet (MP Biomedicals, 152511) solution overnight, and then washed with distilled water before imaging and counting.

For accessing DDR and checkpoint responses via western blot, 2 x 10^6 cells were seeded on a 60 cm dish, allowed to adhere for 24h, and treated with Phleomycin or Hydroxyurea for 3h (drug concentrations are displayed on Figure 2).

Cell culture

HEK-293T cells were cultured in Dulbecco's modified medium supplemented with 10% fetal calf serum, 1% penicillin/streptomycin and 1% nonessential amino acids. Immortalized MEFs were cultured in Dulbecco's modified medium supplemented with 10% fetal calf serum, 1% penicillin/streptomycin, 1% nonessential amino acids, and 1% glutamine supplementation. All cells were kept at 37°C and 5% CO_2. All the cell lines were regularly tested for mycoplasma contamination with the Universal Mycoplasma Detection Kit (ATCC). HEK-293T cells were transfected using homemade polyethylenimine (Polysciences, Inc.). 36h after transfection, cells were treated with 1mM HU (Hydroxyurea) and then harvested for immunoprecipitation experiments.

Plasmids

The full-length TOPBP1 CDS was cloned on a p3xflag vector (Milipore/Sigma E7658) using Gibson assembly (NEB) following the manufacturer's instructions. The p3xflag-TOPBP1 was used as a template to generate p3xflag-TOPBP-K155A, p3xflag-TOPBP-K250A, p3xflag-TOPBP-K704A, p3xflag-TOPBP-K1317A through site-directed mutagenesis using prime STAR master mix (Takara) and Gibson assembly to generate p3xflag-TOPBP-KE, using the following

G-block (IDT) containing the 8 charge-reversal point mutations at the BRCT 5 domain of TOPBP1:
AACGAATCCAATGCAGAAGAAGGCATGTTTGCCAGTACTCATCTTATACTGGAAGA
ACGTGGTGGCTCTGAATATGAAGCTGCAAAGAAGTGGAATTTACCTGCCGTTACTAT
AGCTTGGCTGTTGGAGACTGCTAGAACGGGAGAAGA.
All primers used for the cloning are shown in the key resources table.

Immunoblotting

Cells were harvested and lysed in modified RIPA buffer (50 mM Tris–HCl, pH7.5, 150 mM NaCl, 1% Tergitol, 0.25% sodium deoxycholate, 5 mM ethylenediaminetetraacetic acid (EDTA)) supplemented with complete EDTA-free protease inhibitor cocktail (Roche), 1 mM phenylmethylsulfonyl fluoride (PMSF) and 5 mM NaF. Whole cell lysates, after sonication, were cleared by 15 min centrifugation at 17,000 xg at 4◦C. Twenty micrograms of protein extract were mixed with 3X sodium dodecyl sulfate sample buffer and resolved by SDS-PAGE. Gels were transferred on polyvinylidene difluoride membranes and immunoblotted using standard procedures. Western blot signal was acquired with a Chemidoc Imaging System (BioRad). Antibody information is provided in the key resources table.

Immunofluorescence

MEFs were grown on coverslips and then submitted to IR, 5 gy and allowed to recover for 1.5h at 37°C and 5% CO_2. Cells were then fixed using 3.7% formaldehyde in phosphate-buffered saline (PBS) for 10 min at room temperature (RT). Fixed cells were then washed 3x with PBS, permeabilized for 5 min with 0.2% Triton X-100/PBS at RT and blocked in 10% bovine serum albumin/PBS for 20 min at RT. Coverslips were incubated first with primary antibodies for 2h at RT, followed by three washes with PBS, and then for 1 hour with relative secondary antibodies. After incubation with secondary antibodies, coverslips were washed three times with PBS and then mounted on glass microscope slides using DAPI–Vectashield mounting medium (Vector Laboratories). Slides were imaged on a Leica DMi8 Microscope with a Leica DFC9000 GTC camera using the LAS X (Leica Application Suite X) software with a 100x objective. For micronuclei scoring, ∼150–200 cells/replicate were counted. The two-tailed Student's t-test was used for statistical analysis. Antibody information is provided in the key resources table.

Meiotic Spreads

Meiotic surface spreads were performed from 8- to 12-week-old mice as described by Kolas et al., (Kolas et al., 2005). Briefly, decapsulated testis from mice were incubated on ice in a hypotonic extraction buffer for 45 min. Tubules were then minced into single- cell suspension in 100 mM sucrose, and cells were spread on slides coated with 1% PFA with 0.15% TritionX- 100 and incubated in a humidifying chamber for 4h. For immunostaining, slides were blocked using 10% goat serum and 3% BSA, followed by incubation overnight with primary antibody (listed in the key resources table) at 4°C in a humidifying chamber. Secondary antibodies were incubated at 37°C for 2h in the dark, and slides were then cover-slipped using antifade mounting medium (2.3% DABCO, 20 mM Tris pH 8.0, 8 µg DAPI in 90% glycerol). Slides were imaged on a Leica DMi8 Microscope with a Leica DFC9000 GTC camera using the LAS X (Leica Application Suite X) software. For every condition, a minimum of 50 images from at least two independent mice were acquired. To quantify fluorescence intensity, the LAS X software quantification tool was used as previously described (Sims et al., 2022). Antibody information is provided in the key resources table. p-Values were calculated in Prism - GraphPad using a linear mixed effect model (Nested t test) that takes into account the variability in cells within each mouse when comparing mice between groups (*Topbp1*$^{+/+}$ vs *Topbp1*$^{B5/B5}$).

3D-Structured Illumination super resolution Microscope (3D-SIM)

Higher resolution images were acquired using an ELYRA 3D-Structured Illumination Super Resolution Microscopy (3D-SIM) from Carl Zeiss with ZEN Black software (Carl Zeiss AG, Oberkochen, Germany). Images are shown as maximum intensity projections of z stack images. To reconstruct high-resolution images, raw images were computationally processed by ZEN Black. The brightness and contrast of images were adjusted using ImageJ (National Institutes of Health, USA). Antibody information is provided in the key resources table.

Fertility assays

For fertility testing, 8 weeks old *Topbp1*$^{B5/B5}$ females and C57BL/6 males or C57BL/6 females and *Topbp1*$^{B5/B5}$ males were singly housed, where pregnancies were monitored for a period of one month. Viable pups were counted on the first day of life. For *Topbp1*$^{B5/B5}$ males, breeding cages

remained active for a period of six months and at no time pregnant females nor birth of pups were detected. No noticeable defects were found on fertility of Topbp*1*$^{B5/+}$, males or females (data not shown).

TUNEL

TUNEL assay was conducted using the Apoptag kit (EMD Millipore) following the manufacturer's instructions. The data were quantified in Image Scope by counting the number of positive cells per tubule for 100 tubules of each genotype, 3 mice each. Statistical differences between *Topbp1*$^{+/+}$ and *Topbp1*$^{B5/B5}$ were analyzed using Welch's unpaired t- test in GraphPad.

Hematoxylin and eosin staining

Adult testes - from 12 weeks old mice - were dissected and incubated in Bouin's fixative overnight, washed during 30 min each in 30%, then 50% and then 70% ethanol. The 70% ethanol wash was repeated 3 times more. Testes were then embedded in paraffin. 5 µm sections were mounted on slides. After rehydration in Safe Clear Xylene Substitute followed by decreasing amounts of ethanol, slides were stained with hematoxylin followed by eosin. The slides were then gradually dehydrated by incubation in increasing concentrations of ethanol before mounting using toluene mounting medium.

Epididymal sperm counts

Caudal and epididymides from 8- to 12-week-old mice were minced with fine forceps at 37°C in a Petri dish containing Dulbecco's modified medium supplemented with 10% fetal calf serum, 1% penicillin/streptomycin, 4% BSA, and 1% nonessential amino acids. Samples were then incubated at 37°C for 30 min allowing sperm to swim out into the media, then fixed in 10% neutral-buffered formalin (1:25 dilution). Sperm cells were counted using a hemocytometer and analyzed statistically using the two-tailed Student's t-test between *Topbp1*$^{+/+}$ and *Topbp1*$^{B5/B5}$.

Enrichment of testes phosphopeptides and TMT labeling

The enrichment of testes phosphopeptides and TMT labeling were done as described previously (Sims et al., 2022). Briefly, whole decapsulated testes were collected from 8- to 12-week-old mice after which tissue was subject to lysis, protein quantification and normalization, denaturation,

alkylation, precipitation, digestion, and solid-phase extraction (SPE) C18 cartridge clean up as described by Sims et. al (Sims et al., 2022). Lyophilized tryptic peptides were then subject to phosphopeptide enrichment using a High-Select Fe-NTA Phosphopeptide Enrichment Kit according to the manufacturer's protocol (Cat# A32992, Thermo Scientific). Phosphopeptide samples were dried in silanized glass shell vials, resuspended in 50 mM HEPES, and labeled with 100 µg of TMT sixplex Isobaric Label Reagents (Thermo Scientific) using 3 TMT channels for each condition (*Topbp1*$^{+/+}$ and *Topbp1*$^{B5/B5}$). The TMT-labeling reaction was done at room temperature for 1h and quenched with 5% hydroxylamine for 15 minutes. After quenching, TMT-labeled peptides from all six channels were pooled, acidified with 0.1% TFA, and desalted using a SPE 1cc C18 cartridge (Sep-Pak C18 cc vac cartridge, 50 mg Sorbent, WAT054955, Waters). Bound TMT-labeled phosphopeptides were eluted with 80% acetonitrile, 0.1% acetic acid in water before being dried via vacuum concentrator.

Mass spectrometric analysis of TMT-labeled phosphopeptides

The dried TMT-labeled phosphopeptides were prefractionated using offline HILIC HPLC prior to being analyzed by mass-spectrometry as described by Sims et. al (Sims et al., 2022). The LC-MS/MS was performed on an UltiMate 3000 RSLC nano chromatographic system coupled to a Q-Exactive HF mass spectrometer (Thermo Fisher Scientific). The chromatographic separation was achieved via a 35cm-long 100 µm inner diameter column packed in-house with 3 µm C18 reversed-phase resin (Reprosil Pur C18AQ 3 µm). The Q-Exactive HF was operated in data-dependent mode with survey scans acquired in the Orbitrap mass analyzer over the range of 380–1800 m/z with a mass resolution of 120,000. MS/MS spectra were performed after selecting the top 7 most abundant +2, +3, or +4 ions and a precursor isolation window of 0.7 m/z. Selected ions were fragmented by Higher-energy Collisional Dissociation (HCD) with normalized collision energies of 28, with fragment mass spectra acquired in the Orbitrap mass analyzer with a monitored first mass of 100 m/z, mass resolution of 15,000, AGC target set to 1×10^5, and maximum injection time set to 100 ms. A dynamic exclusion window of 30 seconds was specified.

Phosphoproteomic data analysis

The Trans Proteomic Pipeline (TPP) version 6.0.0 was used for phosphopeptide identification and quantification. MS data were converted to mzXML using msConvert as packaged with the TPP,

after which spectral data files were searched using the Comet search engine (v2021 rev 1) (Eng et al., 2013). Peptide identifications were validated using PeptideProphet, phosphorylation site localization was performed using PTM Prophet, and TMT channel quantification was performed using Libra. Results from Libra were exported as tab-delimited files for further processing via R scripts as previously described (Sims et al., 2022). The mass spectrometry phosphoproteomics data have been deposited to the ProteomeXchange Consortium via the PRIDE [1] partner repository with the dataset identifier PXD042199.

Immunoprecipitation

The immunoprecipitation (IP) experiments were performed as described by Liu et. al (Liu et al., 2017). Briefly, cell pellets were lysed in 50 mM Tris-HCl, pH 7.5, 150 mM NaCl, 1% tergitol, 0.25% sodium deoxycholate, and 5 mM EDTA, supplemented with EDTA-free protease inhibitor cocktail, 5 mM sodium fluoride, 10 mM β-glycerolphosphate, 1 mM PMSF, and 0.4 mM sodium orthovanadate. The protein extracts were cleared by 10-min centrifugation and then were incubated with anti-FLAG agarose beads (Sigma-Aldrich) for 16h at 4°C. The beads were then washed four times with the same buffer used for IP and then eluted using three resin volumes of the elution buffer (100 mM Tris-HCl, pH 8.0, and 1% SDS, and 1 mM DTT).

Mass spectrometric analysis of immunoprecipitates

HEK-293T cells were grown in stable isotope labeling with amino acids in cell culture (SILAC) as previously described (Liu et al., 2017) and transfected as described above. Cells were treated with 1 mM HU for 16h before harvesting. Flag-TOPBP1 was immunoprecipitated using anti-FLAG agarose beads. Immunoprecipitates were then prepared for mass spectrometry analysis by reduction, alkylation, precipitation, and digestion by trypsin. The peptides were desalted, dried, and then fractionated by hydrophilic interaction chromatography as previously described (Liu et al., 2017)). Fractions were dried and analyzed by liquid chromatography–tandem mass spectrometry using a mass spectrometer (Q-Exactive HF Orbitrap; Thermo Fisher Scientific). The capillary column was 35 cm long with a 100-µm inner diameter, packed in-house with 3 µm C18 reversed-phase resin (Reprosil Pur C18AQ 3 µm). Peptides were separated over an 70-minute linear gradient of six to 40% acetonitrile in 0.1% formic acid at a flow rate of 300 nl/min as described previously (Bastos de Oliveira et al., 2015). Xcalibur 2.2 software (Thermo Fischer

Scientific) was used for the data acquisition, and The Q-Exactive HF was operated in data-dependent mode with survey scans acquired in the Orbitrap mass analyzer over the range of 380–1800 m/z with a mass resolution of 120,000. The maximum ion injection time for the survey scan was 100 ms with a 3e6 automatic gain-control target ion. Tandem mass spectrometry spectra were performed by selecting up to the 20 most abundant ions with a charge state of 2, 3, or 4 and with an isolation window of 1.2 m/z. Selected ions were fragmented by higher energy collisional dissociation with a normalized collision energy of 28, and the tandem mass spectra was acquired in the Orbitrap mass analyzer with a mass resolution of 17,500 (at m/z 200). The Trans Proteomic Pipeline (TPP) version 6.0.0 was used for peptide identification and SILAC quantification. MS data were converted to mzXML using msConvert as packaged with the TPP, after which spectral data files were searched using the Comet search engine (v2021 rev 1) (Eng et al., 2013). The following parameters were used in the database search: semitryptic requirement, a mass accuracy of 15 ppm for the precursor ions, a differential modification of 8.0142 D for lysine and 10.00827 D for arginine, and a static mass modification of 57.021465 D for alkylated cysteine residues. Peptide identifications were validated using PeptideProphet and SILAC quantification was performed using XPRESS as described previously (Bastos de Oliveira et al., 2015; Sims et al., 2022). The mass spectrometry data have been deposited to the ProteomeXchange Consortium via the PRIDE [1] partner repository with the dataset identifier PXD042199.

Total germ cells preparation

Mice testis were collected from 8- to 12-week-old mice (n = 5 mice, 10 testis for *Topbp1*$^{+/+}$, and n = 20-30 mice, 40-60 testis for *Topbp1*$^{B5/B5}$), and dissociated using standard protocols for germ cell extraction[73]. Briefly, decapsulated testes were held in 10 ml of preheated (35°C) DMEM-F12 buffer containing 2 mg of Collagenase 1A and DNAse 7 mg/ml, on a 50 ml conical tube. The collagenase digestion was performed at a 35°C shaker water-bath, 150 rpm during 5 min. The collagenase digestion was stopped by the addition of 40 ml of DMEM-F12 and the tubules were let to decantate for 1 min. The supernatant was removed and added another 40 ml of DMEM-F12 to further wash the residual collagenase and remove somatic and excessive sperm cells. Next, the tubules were digested using 10 ml of DMEM-F12 buffer containing 5 mg of trypsin (Thermo Fisher 27250018) on a 50 ml conical tube and the reaction was carried out on a 35°C shaker water-bath, 150 rpm during 5 min. Digested tubules were strained on a 100 μm strainer containing 3 ml

of FBS (100% Fetal Bovine Serum, heat inactivated, Sigma F4135-500mL). Total germ cells were centrifuged at 300 xg for 5 min, 4°C and checked for single cells and viability.

Flow cytometry analysis

Total germ cell extracts were stained with Vybrant dye cycle (VDG) (Invitrogen) 100 μM for 30 min at room temperature, kept on dark, and rocking. After staining, cells were sorted as previously described (Rodríguez-Casuriaga et al., 2014) aiming to enrich for spermatocytes, and using the Sony MA900 fluorescent activated cell sorter (FACS), tuned to emit at 488 nm and with a 100 μm nozzle. Laser power was set to collect VDG-emitted fluorescence in FL1. Sorted cells were collected on 1.5 ml tubes containing 0.5 ml of DMEM-F12 buffer + 10% FBS. The FACS was done at the Flow Cytometry Facility - Cornell University.

Single-Cell RNA sequencing

Flow sorted cells were submitted to the Cornell DNA Sequencing Core Facility and processed on the 10X Genomics Chromium System targeting 5000–7000 cells per sample as described previously (Grive et al., 2019) using the 10X Genomics Chromium Single Cell 3′ RNA-seq v2 kit to generate the sequencing libraries, which were then tested for quality control on an ABI DNA Fragment Analyzer and ran on a NextSeq platform with 150 base-pair reads. The sequencing was carried out to an average depth of 98M reads (range 77M-124M); on average, 91% of reads (range 89%-92%) and then mapped to the reference genome.

Single-cell RNA sequencing data analysis

Count matrices were generated for each sample using the Cell Ranger counts function and then imported into Seurat and integrated. Cells were filtered based on gene number, UMI, counts, and mitochondrial percentage. Cells with less than 500 genes, less than 1000 UMIs, or more than 5% of mitochondrial reads were excluded from further analysis (Supplemental Figure 29). Raw counts were normalized using Seurat NormalizeData using default parameters and the top 4000 variable features were identified using the FindVariableFeatures function using ExpMean for the mean function and LogVMR for the dispersion function. Principal components were calculated from variable genes and used with Harmony to correct for batch effect. Harmony embeddings dimensions 1-20 were used for a Shared Nearest Neighbor graph with k=30, unsupervised

clustering with a resolution of 4, and Uniform Manifold Approximation and Projection (UMAP) analysis. Cell types were manually identified by use of marker genes, and the SingleR package was used to confirm cell identity. Chromosome X/autosome 9 ratios were calculated by taking the mean gene expression of all genes on chromosome 9 or X for a cell and dividing it by the mean gene expression for all autosomal genes in a cell. Ratios were visualized using ggplot and the introdataviz package geom_split_violin function. The single cell heatmap was generated using the DoHeatmap function. The clustered analysis of the X-linked genes shown in Figure 7A, was done by splitting the detected 233 X-linked genes into 3 distinct categories based on the difference of RNA level between the spermatocyte stages and normalized by pre-leptotene: reduced silencing (> 1), unaltered silencing (≥ -1 or ≤ 1), or increased silencing (< -1). To further split the X-linked genes into 3 categories based on the severity of the silencing defect (detected at spermatocyte 3 stage) in *Topbp1*$^{B5/B5}$: no defect (13 genes), mild (45 genes) or strong defect (170 genes), the difference in expression between SP3 genes from *Topbp1*$^{+/+}$ or from *Topbp1*$^{B5/B5}$ was calculated. The categories were defined as: Strong > 2.5, Mild ≥ 1 or ≤ 2.5 and no defect <1. The Single-cell RNAseq data generated in this study have been deposited in the NCBI GEO database under accession number GSE232588.

Data and code availability

All data and original codes reported in this work, and any additional information required will be shared by the lead contact upon request.

Acknowledgments

We thank the members of Cohen lab, Weiss lab, Grimson lab and Smolka lab for comments and suggestions. We thank Dr. Fenghua Hu and Dr. Tony Bretscher for the use of the microscopes and Beatriz Almeida for technical assistance. We thank Dr. Lydia Tesfa and the BRC Flow Cytometry Facility (RRID:SCR_021740) for training and assistance with FACS at the Cornell Institute of Biotechnology, Peter Schweitzer and the BRC Genomics Facility (RRID:SCR_021727) at the Cornell Institute of Biotechnology for sequencing experiments, Johana M. de la Cruz and the BRC Imaging Facility (RRID:SCR_021741) at the Cornell Institute of Biotechnology for training and assistance with the Elyra Super Resolution Microscope and the 3D-SIM imaging. We thank Marco Hiler and the BMS and Stem Cell Pathology Unit at the Cornell Veterinary Research Tower for

training and assistance with imaging histological sections using ScanScope. We thank Dr. John Schimenti, Dr. Robert Munroe, Mr. Christian Abratte, and Cornell's Stem Cell and Transgenic Core Facility for generating the *Topbp1*$^{B5/B5}$ mouse. We thank Dr. Mary Ann Handel for the H1T antibody.

Author contributions

M.B.S, C.F.R.A and J.R.S. conceived the project. M.B.S and C.F.R.A wrote the paper. C.F.R.A and J.R.S contributed equally with conceptualization, data curation and formal analysis. C.F.R.A, J.R.S and E.A.F. performed experiments. A.D and A.G contributed with data curation and formal analysis. W.C and J.B contributed with data analysis. M.B.S, C.F.R.A, R.W. and P.E.C, contributed with funding acquisition. R.F. contributed with resources.

Declaration of interests

No competing interests declared.

Inclusion and diversity

We support inclusive, diverse, and equitable conduct of research.

Funding

This work was supported by Eunice Kennedy Shriver National Institute of Child Health and Human Development (R01-HD095296) to M.B.S and R.W, National Institute of Health – General Medicine (R35-GM141159) to M.B.S, National Institute of Health (R01HD041012) to P.E.C, the Eunice Kennedy Shriver National Institute of Child Health and Human Development (P50HD104454) to A.G., the Spanish Agencia Estatal de Investigación [PID2019-109222RB-I00/AEI/10.13039/501100011033]; European Union Regional Funds (FEDER) to R. F., and 2022 CVG Scholar Award from the Center of Vertebrates Genomics and the 2022 ASCB International training Scholarship to C.F.R.A.

References

Abe H, Alavattam KG, Hu Y-C, Pang Q, Andreassen PR, Hegde RS, Namekawa SH. 2020. The Initiation of Meiotic Sex Chromosome Inactivation Sequesters DNA Damage Signaling from Autosomes in Mouse Spermatogenesis. *Curr Biol* **30**:408-420.e5. doi:10.1016/j.cub.2019.11.064

Abe H, Alavattam KG, Kato Y, Castrillon DH, Pang Q, Andreassen PR, Namekawa SH. 2018. CHEK1 coordinates DNA damage signaling and meiotic progression in the male germline of mice. *Hum Mol Genet* **27**:1136–1149. doi:10.1093/hmg/ddy022

Abe H, Yeh Y-H, Munakata Y, Ishiguro K-I, Andreassen PR, Namekawa SH. 2022. Active DNA damage response signaling initiates and maintains meiotic sex chromosome inactivation. *Nat Commun* **13**:7212. doi:10.1038/s41467-022-34295-5

Alavattam KG, Abe H, Sakashita A, Namekawa SH. 2018. Chromosome spread analyses of meiotic sex chromosome inactivationMethods in Molecular Biology. Humana Press Inc. pp. 113–129. doi:10.1007/978-1-4939-8766-5_10

Alavattam KG, Maezawa S, Andreassen PR, Namekawa SH. 2022. Meiotic sex chromosome inactivation and the XY body: a phase separation hypothesis. *Cellular and Molecular Life Sciences*. doi:10.1007/s00018-021-04075-3

Aran D, Looney AP, Liu L, Wu E, Fong V, Hsu A, Chak S, Naikawadi RP, Wolters PJ, Abate AR, Butte AJ, Bhattacharya M. 2019. Reference-based analysis of lung single-cell sequencing reveals a transitional profibrotic macrophage. *Nat Immunol* **20**:163–172. doi:10.1038/s41590-018-0276-y

Balbo Pogliano C, Ceppi I, Giovannini S, Petroulaki V, Palmer N, Uliana F, Gatti M, Kasaciunaite K, Freire R, Seidel R, Altmeyer M, Cejka P, Matos J. 2022. The CDK1-TOPBP1-PLK1 axis regulates the Bloom's syndrome helicase BLM to suppress crossover recombination in somatic cells. *Sci Adv* **8**:eabk0221. doi:10.1126/sciadv.abk0221

Balmus G, Zhu M, Mukherjee S, Lyndaker AM, Hume KR, Lee J, Riccio ML, Reeves AP, Sutter NB, Noden DM, Peters RM, Weiss RS. 2012. Disease severity in a mouse model of ataxia telangiectasia is modulated by the DNA damage checkpoint gene Hus1. *Hum Mol Genet* **21**:3408–3420. doi:10.1093/hmg/dds173

Bastos de Oliveira FM, Kim D, Cussiol JR, Das J, Jeong MC, Doerfler L, Schmidt KH, Yu H, Smolka MB. 2015. Phosphoproteomics reveals distinct modes of Mec1/ATR signaling during DNA replication. *Mol Cell* **57**:1124–1132. doi:10.1016/j.molcel.2015.01.043

Becherel OJ, Yeo AJ, Stellati A, Heng EYH, Luff J, Suraweera AM, Woods R, Fleming J, Carrie D, McKinney K, Xu X, Deng C, Lavin MF. 2013. Senataxin Plays an Essential Role with DNA Damage Response Proteins in Meiotic Recombination and Gene Silencing. *PLoS Genet* **9**. doi:10.1371/journal.pgen.1003435

Bennett CL, La Spada AR. 2018. Senataxin, A Novel Helicase at the Interface of RNA Transcriptome Regulation and Neurobiology: From Normal Function to Pathological Roles in Motor Neuron Disease and Cerebellar Degeneration In: Sattler R, Donnelly CJ, editors. RNA Metabolism in Neurodegenerative Diseases. Cham: Springer International Publishing. pp. 265–281. doi:10.1007/978-3-319-89689-2_10

Bigot N, Day M, Baldock RA, Watts FZ, Oliver AW, Pearl LH. 2019. Phosphorylation-mediated

926 interactions with topbp1 couple 53bp1 and 9-1-1 to control the g1 DNA damage
927 checkpoint. *Elife* **8**:1–28. doi:10.7554/eLife.44353
928 Blackford AN, Jackson SP. 2017. ATM, ATR, and DNA-PK: The Trinity at the Heart of the DNA
929 Damage Response. *Mol Cell* **66**:801–817. doi:10.1016/j.molcel.2017.05.015
930 Blackford AN, Nieminuszczy J, Schwab RA, Galanty Y, Jackson SP, Niedzwiedz W. 2015. TopBP1
931 Interacts with BLM to Maintain Genome Stability but Is Dispensable for Preventing BLM
932 Degradation. *Mol Cell* **57**:1133–1141. doi:10.1016/j.molcel.2015.02.012
933 Broering TJ, Alavattam KG, Sadreyev RI, Ichijima Y, Kato Y, Hasegawa K, Camerini-Otero RD, Lee
934 JT, Andreassen PR, Namekawa SH. 2014. BRCA1 establishes DNA damage signaling and
935 pericentric heterochromatin of the X chromosome in male meiosis. *J Cell Biol* **205**:663–
936 675. doi:10.1083/jcb.201311050
937 Brown EJ, Baltimore D. 2000. ATR disruption leads to chromosomal fragmentation and early
938 embryonic lethality. *Genes and Development* **14**. doi:10.1101/gad.14.4.397
939 Burgoyne PS, Mahadevaiah SK, Turner JMA. 2009. The consequences of asynapsis for mammalian
940 meiosis. *Nature Reviews Genetics*. doi:10.1038/nrg2505
941 Carlson M, Falcon S, Pages H, Li N. n.d. org. Mm. eg. db: Genome wide annotation for Mouse. *R*
942 *package version*.
943 Carpenter AT. 1979. Recombination nodules and synaptonemal complex in recombination-
944 defective females of Drosophila melanogaster. *Chromosoma* **75**:259–292.
945 doi:10.1007/BF00293472
946 Cescutti R, Negrini S, Kohzaki M, Halazonetis TD. 2010. TopBP1 functions with 53BP1 in the G1
947 DNA damage checkpoint. *EMBO J* **29**:3723–3732. doi:10.1038/emboj.2010.238
948 Chen Y, Zheng Y, Gao Y, Lin Z, Yang S, Wang T, Wang Q, Xie N, Hua R, Liu M, Sha J, Griswold MD,
949 Li J, Tang F, Tong M-H. 2018. Single-cell RNA-seq uncovers dynamic processes and critical
950 regulators in mouse spermatogenesis. *Cell Res* **28**:879–896. doi:10.1038/s41422-018-
951 0074-y
952 Cimprich KA, Cortez D. 2008. ATR: An essential regulator of genome integrity. *Nature Reviews*
953 *Molecular Cell Biology*. doi:10.1038/nrm2450
954 Cohen S, Puget N, Lin Y-L, Clouaire T, Aguirrebengoa M, Rocher V, Pasero P, Canitrot Y, Legube G.
955 2018. Senataxin resolves RNA:DNA hybrids forming at DNA double-strand breaks to
956 prevent translocations. *Nat Commun* **9**:533. doi:10.1038/s41467-018-02894-w
957 Danielsen JMR, Larsen DH, Freire R, Falck J, Bartek J, Lukas J, Others. 2009. HCLK2 is required for
958 activity of the DNA damage response kinase ATR. *J Biol Chem* **284**:4140–4147.
959 De Klein A, Muijtjens M, Van Os R, Verhoeven Y, Smit B, Carr AM, Lehmann AR, Hoeijmakers JHJ.
960 2000. Targeted disruption of the cell-cycle checkpoint gene ATR leads to early embryonic
961 lethality in mice. *Curr Biol* **10**. doi:10.1016/S0960-9822(00)00447-4
962 Delacroix S, Wagner JM, Kobayashi M, Yamamoto KI, Karnitz LM. 2007. The Rad9-Hus1-Rad1 (9-
963 1-1) clamp activates checkpoint signaling via TopBP1. *Genes and Development* **21**:1472–
964 1477. doi:10.1101/gad.1547007
965 Durinck S, Spellman PT, Birney E, Huber W. 2009. Mapping identifiers for the integration of
966 genomic datasets with the R/Bioconductor package biomaRt. *Nat Protoc* **4**:1184–1191.
967 doi:10.1038/nprot.2009.97
968 ElInati E, Russell HR, Ojarikre OA, Sangrithi M, Hirota T, De Rooij DG, McKinnon PJ, Turner JMA.
969 2017. DNA damage response protein TOPBP1 regulates X chromosome silencing in the

970 mammalian germ line. *Proc Natl Acad Sci U S A* **114**:12536–12541.
971 doi:10.1073/pnas.1712530114
972 Eng JK, Jahan TA, Hoopmann MR. 2013. Comet: An open-source MS/MS sequence database
973 search tool. *PROTEOMICS*. doi:10.1002/pmic.201200439
974 Falck J, Coates J, Jackson SP. 2005. Conserved modes of recruitment of ATM, ATR and DNA-PKcs
975 to sites of DNA damage. *Nature* **434**:605–611. doi:10.1038/nature03442
976 Fanning E, Klimovich V, Nager AR. 2006. A dynamic model for replication protein A (RPA) function
977 in DNA processing pathways. *Nucleic Acids Res* **34**:4126–4137. doi:10.1093/nar/gkl550
978 Gray S, Cohen PE. 2016. Control of Meiotic Crossovers: From Double-Strand Break Formation to
979 Designation. *Annu Rev Genet* **50**:175–210. doi:10.1146/annurev-genet-120215-035111
980 Greenlee AR, Shiao M-S, Snyder E, Buaas FW, Gu T, Stearns TM, Sharma M, Murchison EP, Puente
981 GC, Braun RE. 2012. Deregulated sex chromosome gene expression with male germ cell-
982 specific loss of Dicer1. *PLoS One* **7**:e46359. doi:10.1371/journal.pone.0046359
983 Grive KJ, Hu Y, Shu E, Grimson A, Elemento O, Grenier JK, Cohen PE. 2019. Dynamic transcriptome
984 profiles within spermatogonial and spermatocyte populations during postnatal testis
985 maturation revealed by single-cell sequencing. *PLoS Genet* **15**:e1007810.
986 doi:10.1371/journal.pgen.1007810
987 Handel MA, Schimenti JC. 2010. Genetics of mammalian meiosis: regulation, dynamics and
988 impact on fertility. *Nat Rev Genet* **11**:124–136. doi:10.1038/nrg2723
989 Hao Y, Hao S, Andersen-Nissen E, Mauck WM 3rd, Zheng S, Butler A, Lee MJ, Wilk AJ, Darby C,
990 Zager M, Hoffman P, Stoeckius M, Papalexi E, Mimitou EP, Jain J, Srivastava A, Stuart T,
991 Fleming LM, Yeung B, Rogers AJ, McElrath JM, Blish CA, Gottardo R, Smibert P, Satija R.
992 2021. Integrated analysis of multimodal single-cell data. *Cell* **184**:3573-3587.e29.
993 doi:10.1016/j.cell.2021.04.048
994 Hartwell LH, Kastan MB. 1994. Cell cycle control and cancer. *Science* **266**:1821–1828.
995 doi:10.1126/science.7997877
996 Hirota T, Blakeley P, Sangrithi MN, Mahadevaiah SK, Encheva V, Snijders AP, ElInati E, Ojarikre
997 OA, de Rooij DG, Niakan KK, Turner JMA. 2018. SETDB1 Links the Meiotic DNA Damage
998 Response to Sex Chromosome Silencing in Mice. *Dev Cell* **47**:645-659.e6.
999 doi:10.1016/j.devcel.2018.10.004
1000 Holloway JK, Morelli MA, Borst PL, Cohen PE. 2010. Mammalian BLM helicase is critical for
1001 integrating multiple pathways of meiotic recombination. *J Cell Biol* **188**:779–789.
1002 doi:10.1083/jcb.200909048
1003 Holloway JK, Sun X, Yokoo R, Villeneuve AM, Cohen PE. 2014. Mammalian CNTD1 is critical for
1004 meiotic crossover maturation and deselection of excess precrossover sites. *J Cell Biol*
1005 **205**:633–641. doi:10.1083/jcb.201401122
1006 Ichijima Y, Ichijima M, Lou Z, Nussenzweig A, Daniel Camerini-Otero R, Chen J, Andreassen PR,
1007 Namekawa SH. 2011. MDC1 directs chromosome-wide silencing of the sex chromosomes
1008 in male germ cells. *Genes and Development* **25**:959–971. doi:10.1101/gad.2030811
1009 Ichijima Y, Sin HS, Namekawa SH. 2012. Sex chromosome inactivation in germ cells: Emerging
1010 roles of DNA damage response pathways. *Cellular and Molecular Life Sciences*.
1011 doi:10.1007/s00018-012-0941-5
1012 Inselman A, Eaker S, Handel MA. 2003. Temporal expression of cell cycle-related proteins during
1013 spermatogenesis: establishing a timeline for onset of the meiotic divisions. *Cytogenet*

1014 *Genome Res* **103**:277–284. doi:10.1159/000076813
1015 Jeon Y, Ko E, Lee KY, Ko MJ, Park SY, Kang J, Jeon CH, Lee H, Hwang DS. 2011. TopBP1 deficiency
1016 causes an early embryonic lethality and induces cellular senescence in primary cells. *J Biol*
1017 *Chem* **286**:5414–5422. doi:10.1074/jbc.M110.189704
1018 Jeon Y, Park MK, Kim SM, Bae JS, Lee CW, Lee H. 2019. TopBP1 deficiency impairs the localization
1019 of proteins involved in early recombination and results in meiotic chromosome defects
1020 during spermatogenesis. *Biochem Biophys Res Commun* **508**:722–728.
1021 doi:10.1016/j.bbrc.2018.12.001
1022 Joshi N, Brown MS, Bishop DK, Börner GV. 2015. Gradual Implementation of the Meiotic
1023 Recombination Program via Checkpoint Pathways Controlled by Global DSB Levels. *Mol*
1024 *Cell* **57**. doi:10.1016/j.molcel.2014.12.027
1025 Jung M, Wells D, Rusch J, Ahmad S, Marchini J, Myers SR, Conrad DF. 2019. Unified single-cell
1026 analysis of testis gene regulation and pathology in five mouse strains. *eLife*.
1027 doi:10.7554/elife.43966
1028 Kakarougkas A, Ismail A, Katsuki Y, Freire R, Shibata A, Jeggo PA. 2013. Co-operation of BRCA1
1029 and POH1 relieves the barriers posed by 53BP1 and RAP80 to resection. *Nucleic Acids Res*
1030 **41**:10298–10311. doi:10.1093/nar/gkt802
1031 Kassambara A. 2019. GGPlot2 Essentials: Great Data Visualization in R. Independently Published.
1032 Keeney S, Giroux CN, Kleckner N. 1997. Meiosis-specific DNA double-strand breaks are catalyzed
1033 by Spo11, a member of a widely conserved protein family. *Cell* **88**. doi:10.1016/S0092-
1034 8674(00)81876-0
1035 Khalil AM, Boyar FZ, Driscoll DJ. 2004. Dynamic histone modifications mark sex chromosome
1036 inactivation and reactivation during mammalian spermatogenesis. *Proc Natl Acad Sci U S*
1037 *A* **101**:16583–16587. doi:10.1073/pnas.0406325101
1038 Kolas NK, Svetlanov A, Lenzi ML, Macaluso FP, Lipkin SM, Liskay RM, Greally J, Edelmann W,
1039 Cohen PE. 2005. Localization of MMR proteins on meiotic chromosomes in mice indicates
1040 distinct functions during prophase I. *J Cell Biol* **171**:447–458. doi:10.1083/jcb.200506170
1041 Korsunsky I, Millard N, Fan J, Slowikowski K, Zhang F, Wei K, Baglaenko Y, Brenner M, Loh P-R,
1042 Raychaudhuri S. 2019. Fast, sensitive and accurate integration of single-cell data with
1043 Harmony. *Nat Methods* **16**:1289–1296. doi:10.1038/s41592-019-0619-0
1044 Kumagai A, Lee J, Yoo HY, Dunphy WG. 2006. TopBP1 activates the ATR-ATRIP complex. *Cell*
1045 **124**:943–955. doi:10.1016/j.cell.2005.12.041
1046 Kwon M, Leibowitz ML, Lee J-H. 2020. Small but mighty: the causes and consequences of
1047 micronucleus rupture. *Experimental & Molecular Medicine*. doi:10.1038/s12276-020-
1048 00529-z
1049 Lanz MC, Dibitetto D, Smolka MB. 2019. DNA damage kinase signaling: checkpoint and repair at
1050 30 years. *EMBO J* **38**:e101801. doi:10.15252/embj.2019101801
1051 Lau X, Munusamy P, Ng MJ, Sangrithi M. 2020. Single-Cell RNA Sequencing of the Cynomolgus
1052 Macaque Testis Reveals Conserved Transcriptional Profiles during Mammalian
1053 Spermatogenesis. *Dev Cell* **54**:548-566.e7. doi:10.1016/j.devcel.2020.07.018
1054 Leek JT, Johnson WE, Parker HS, Fertig EJ, Jaffe AE. n.d. sva: Surrogate Variable Analysis R package
1055 version 3.10. 0. *DOI10 B*.
1056 Leimbacher PA, Jones SE, Shorrocks AMK, de Marco Zompit M, Day M, Blaauwendraad J,
1057 Bundschuh D, Bonham S, Fischer R, Fink D, Kessler BM, Oliver AW, Pearl LH, Blackford AN,

1058 Stucki M. 2019. MDC1 Interacts with TOPBP1 to Maintain Chromosomal Stability during
1059 Mitosis. *Mol Cell* **74**:571-583.e8. doi:10.1016/j.molcel.2019.02.014
1060 Lenzi ML, Smith J, Snowden T, Kim M, Fishel R, Poulos BK, Cohen PE. 2005. Extreme heterogeneity
1061 in the molecular events leading to the establishment of chiasmata during meiosis i in
1062 human oocytes. *Am J Hum Genet* **76**:112–127. doi:10.1086/427268
1063 Leung CCY, Gong Z, Chen J, Glover JNM. 2011. Molecular basis of BACH1/FANCJ recognition by
1064 TopBP1 in DNA replication checkpoint control. *J Biol Chem* **286**:4292–4301.
1065 doi:10.1074/jbc.M110.189555
1066 Lipkin SM, Wang V, Jacoby R, Banerjee-Basu S, Baxevanis AD, Lynch HT, Elliott RM, Collins FS.
1067 2000. MLH3: a DNA mismatch repair gene associated with mammalian microsatellite
1068 instability. *Nat Genet* **24**:27–35. doi:10.1038/71643
1069 Liu Y, Cussiol JR, Dibitetto D, Sims JR, Twayana S, Weiss RS, Freire R, Marini F, Pellicioli A, Smolka
1070 MB. 2017. TOPBP1Dpb11 plays a conserved role in homologous recombination DNA
1071 repair through the coordinated recruitment of 53BP1Rad9. *J Cell Biol* **216**:623–639.
1072 doi:10.1083/jcb.201607031
1073 Manke IA, Lowery DM, Nguyen A, Yaffe MB. 2003. BRCT repeats as phosphopeptide-binding
1074 modules involved in protein targeting. *Science* **302**:636–639.
1075 doi:10.1126/science.1088877
1076 Maréchal A, Zou L. 2013. DNA damage sensing by the ATM and ATR kinases. *Cold Spring Harb*
1077 *Perspect Biol* **5**. doi:10.1101/cshperspect.a012716
1078 Marnef A, Legube G. 2020. m6A RNA modification as a new player in R-loop regulation. *Nat*
1079 *Genet*. doi:10.1038/s41588-019-0563-z
1080 Modzelewski AJ, Hilz S, Crate EA, Schweidenback CTH, Fogarty EA, Grenier JK, Freire R, Cohen PE,
1081 Grimson A. 2015. Dgcr8 and Dicer are essential for sex chromosome integrity during
1082 meiosis in males. *J Cell Sci* **128**:2314–2327. doi:10.1242/jcs.167148
1083 Modzelewski AJ, Holmes RJ, Hilz S, Grimson A, Cohen PE. 2012. AGO4 regulates entry into meiosis
1084 and influences silencing of sex chromosomes in the male mouse germline. *Dev Cell*
1085 **23**:251–264. doi:10.1016/j.devcel.2012.07.003
1086 Moens PB, Tarsounas M, Morita T, Habu T, Rottinghaus ST, Freire R, Jackson SP, Barlow C,
1087 Wynshaw-Boris A. 1999. The association of ATR protein with mouse meiotic chromosome
1088 cores. *Chromosoma* **108**. doi:10.1007/s004120050356
1089 Monesi V. 1965. Differential rate of ribonucleic acid synthesis in the autosomes and sex
1090 chromosomes during male meiosis in the mouse. *Chromosoma* **17**:11–21.
1091 doi:10.1007/bf00285153
1092 Mordes DA, Glick GG, Zhao R, Cortez D. 2008. TopBP1 activates ATR through ATRIP and a PIKK
1093 regulatory domain. *Genes and Development* **22**:1478–1489. doi:10.1101/gad.1666208
1094 Nakagawa T, Datta A, Kolodner RD. 1999. Multiple functions of MutS- and MutL-related
1095 heterocomplexes. *Proc Natl Acad Sci U S A*. doi:10.1073/pnas.96.25.14186
1096 O'Driscoll M. 2009. Mouse models for ATR deficiency. *DNA Repair* **8**.
1097 doi:10.1016/j.dnarep.2009.09.001
1098 O'Driscoll M, Dobyns WB, Van Hagen JM, Jeggo PA. 2007. Cellular and clinical impact of
1099 haploinsufficiency for genes involved in ATR signaling. *Am J Hum Genet* **81**.
1100 doi:10.1086/518696
1101 Pacheco S, Maldonado-Linares A, Marcet-Ortega M, Rojas C, Martínez-Marchal A, Fuentes-Lazaro

1102 J, Lange J, Jasin M, Keeney S, Fernández-Capetillo O, Garcia-Caldés M, Roig I. 2018. ATR is
1103 required to complete meiotic recombination in mice. *Nat Commun* **9**.
1104 doi:10.1038/s41467-018-04851-z
1105 Parrilla-Castellar ER, Arlander SJH, Karnitz L. 2004. Dial 9–1–1 for DNA damage: the Rad9–Hus1–
1106 Rad1 (9–1–1) clamp complex. *DNA Repair* **3**:1009–1014.
1107 doi:10.1016/j.dnarep.2004.03.032
1108 Pereira C, Arroyo-Martinez GA, Guo MZ, Downey MS, Kelly ER, Grive KJ, Mahadevaiah SK, Sims
1109 JR, Faca VM, Tsai C, Schiltz CJ, Wit N, Jacobs H, Clark NL, Freire R, Turner J, Lyndaker AM,
1110 Brieno-Enriquez MA, Cohen PE, Smolka MB, Weiss RS. 2022. Multiple 9-1-1 complexes
1111 promote homolog synapsis, DSB repair, and ATR signaling during mammalian meiosis.
1112 *Elife* **11**. doi:10.7554/eLife.68677
1113 Pereira C, Smolka MB, Weiss RS, Brieño-Enríquez MA. 2020. ATR signaling in mammalian meiosis:
1114 From upstream scaffolds to downstream signaling. *Environ Mol Mutagen* **61**:752–766.
1115 doi:10.1002/em.22401
1116 Perera D, Perez-Hidalgo L, Moens PB, Reini K, Lakin N, Syväoja JE, San-Segundo PA, Freire R. 2004.
1117 TopBP1 and ATR Colocalization at Meiotic Chromosomes: Role of TopBP1/Cut5 in the
1118 Meiotic Recombination Checkpoint. *Mol Biol Cell* **15**:1568–1579. doi:10.1091/mbc.E03-
1119 06
1120 Reini K, Uitto L, Perera D, Moens PB, Freire R, Syväoja JE. 2004. TopBPI localises to centrosomes
1121 in mitosis and to chromosome cores in meiosis. *Chromosoma* **112**. doi:10.1007/s00412-
1122 004-0277-5
1123 Rockmill B, Fung JC, Branda SS, Roeder GS. 2003. The Sgs1 helicase regulates chromosome
1124 synapsis and meiotic crossing over. *Curr Biol* **13**:1954–1962.
1125 doi:10.1016/j.cub.2003.10.059
1126 Rodriguez M, Yu X, Chen J, Songyang Z. 2003. Phosphopeptide binding specificities of BRCA1
1127 COOH-terminal (BRCT) domains. *J Biol Chem* **278**:52914–52918.
1128 doi:10.1074/jbc.C300407200
1129 Rodríguez-Casuriaga R, Santiñaque FF, Folle GA, Souza E, López-Carro B, Geisinger A. 2014. Rapid
1130 preparation of rodent testicular cell suspensions and spermatogenic stages purification
1131 by flow cytometry using a novel blue-laser-excitable vital dye. *MethodsX* **1**:239–243.
1132 doi:10.1016/j.mex.2014.10.002
1133 Royo H, Polikiewicz G, Mahadevaiah SK, Prosser H, Mitchell M, Bradley A, De Rooij DG, Burgoyne
1134 PS, Turner JMA. 2010. Evidence that meiotic sex chromosome inactivation is essential for
1135 male fertility. *Curr Biol* **20**:2117–2123. doi:10.1016/j.cub.2010.11.010
1136 Royo H, Prosser H, Ruzankina Y, Mahadevaiah SK, Cloutier JM, Baumann M, Fukuda T, Höög C,
1137 Tóth A, de Rooij DG, Bradley A, Brown EJ, Turner JMA. 2013. ATR acts stage specifically to
1138 regulate multiple aspects of mammalian meiotic silencing. *Genes and Development* **27**.
1139 doi:10.1101/gad.219477.113
1140 Santos-Pereira JM, Aguilera A. 2015. R loops: new modulators of genome dynamics and function.
1141 *Nat Rev Genet* **16**:583–597. doi:10.1038/nrg3961
1142 Shiloh Y. 2003. ATM and related protein kinases: safeguarding genome integrity. *Nat Rev Cancer*
1143 **3**:155–168. doi:10.1038/nrc1011
1144 Shin Y-H, Choi Y, Erdin SU, Yatsenko SA, Kloc M, Yang F, Jeremy Wang P, Meistrich ML, Rajkovic
1145 A. 2010. Hormad1 Mutation Disrupts Synaptonemal Complex Formation, Recombination,

1146 and Chromosome Segregation in Mammalian Meiosis. *PLoS Genetics*.
1147 doi:10.1371/journal.pgen.1001190
1148 Sims JR, Faça VM, Pereira C, Ascenção C, Comstock W, Badar J, Arroyo-Martinez GA, Freire R,
1149 Cohen PE, Weiss RS, Smolka MB. 2022. Phosphoproteomics of ATR signaling in mouse
1150 testes. *Elife* **11**. doi:10.7554/eLife.68648
1151 Solari AJ. 1974. The behavior of the XY pair in mammals. *Int Rev Cytol* **38**:273–317.
1152 doi:10.1016/s0074-7696(08)60928-6
1153 Subramanian VV, Hochwagen A. 2014. The meiotic checkpoint network: step-by-step through
1154 meiotic prophase. *Cold Spring Harb Perspect Biol* **6**:a016675.
1155 doi:10.1101/cshperspect.a016675
1156 Svetlanov A, Baudat F, Cohen PE, de Massy B. 2008. Distinct functions of MLH3 at recombination
1157 hot spots in the mouse. *Genetics* **178**:1937–1945. doi:10.1534/genetics.107.084798
1158 Thompson A, Schäfer J, Kuhn K, Kienle S, Schwarz J, Schmidt G, Neumann T, Johnstone R,
1159 Mohammed AKA, Hamon C. 2003. Tandem mass tags: a novel quantification strategy for
1160 comparative analysis of complex protein mixtures by MS/MS. *Anal Chem* **75**:1895–1904.
1161 doi:10.1021/ac0262560
1162 Turner JMA. 2015. Meiotic Silencing in Mammals. *Annu Rev Genet* **49**. doi:10.1146/annurev-
1163 genet-112414-055145
1164 Turner JMA. 2007. Meiotic sex chromosome inactivation. *Development* **134**:1823–1831.
1165 doi:10.1242/dev.000018
1166 Turner JMA, Aprelikova O, Xu X, Wang R, Kim S, Chandramouli GVR, Barrett JC, Burgoyne PS, Deng
1167 C-X. 2004. BRCA1, histone H2AX phosphorylation, and male meiotic sex chromosome
1168 inactivation. *Curr Biol* **14**:2135–2142. doi:10.1016/j.cub.2004.11.032
1169 Turner JMA, Mahadevaiah SK, Ellis PJI, Mitchell MJ, Burgoyne PS. 2006. Pachytene asynapsis
1170 drives meiotic sex chromosome inactivation and leads to substantial postmeiotic
1171 repression in spermatids. *Dev Cell* **10**:521–529. doi:10.1016/j.devcel.2006.02.009
1172 Vernet N, Mahadevaiah SK, de Rooij DG, Burgoyne PS, Ellis PJI. 2016. Zfy genes are required for
1173 efficient meiotic sex chromosome inactivation (MSCI) in spermatocytes. *Hum Mol Genet*
1174 **25**:5300–5310. doi:10.1093/hmg/ddw344
1175 Wang J, Chen J, Gong Z. 2013. TopBP1 controls BLM protein level to maintain genome stability.
1176 *Mol Cell* **52**:667–678. doi:10.1016/j.molcel.2013.10.012
1177 Wang J, Gong Z, Chen J. 2011. MDC1 collaborates with TopBP1 in DNA replication checkpoint
1178 control. *J Cell Biol* **193**:267–273. doi:10.1083/jcb.201010026
1179 Wei T, Simko V. 2017. R package "corrplot": Visualization of a Correlation Matrix (Version 0.84).
1180 Wickham H. 2007. Reshaping Data with the reshape Package. *J Stat Softw* **21**:1–20.
1181 doi:10.18637/jss.v021.i12
1182 Wickham H, Averick M, Bryan J, Chang W, McGowan L, François R, Grolemund G, Hayes A, Henry
1183 L, Hester J, Kuhn M, Pedersen T, Miller E, Bache S, Müller K, Ooms J, Robinson D, Seidel
1184 D, Spinu V, Takahashi K, Vaughan D, Wilke C, Woo K, Yutani H. 2019. Welcome to the
1185 tidyverse. *J Open Source Softw* **4**:1686. doi:10.21105/joss.01686
1186 Widger A, Mahadevaiah SK, Lange J, Elinati E, Zohren J, Hirota T, Pacheco S, Maldonado-Linares
1187 A, Stanzione M, Ojarikre O, Maciulyte V, De Rooij DG, Tóth A, Roig I, Keeney S, Turner
1188 JMA. 2018. ATR is a multifunctional regulator of male mouse meiosis. *Nat Commun* **9**.
1189 doi:10.1038/s41467-018-04850-0

1190 Wojtasz L, Cloutier JM, Baumann M, Daniel K, Varga J, Fu J, Anastassiadis K, Stewart AF, Reményi
1191 A, Turner JMA, Tóth A. 2012. Meiotic DNA double-strand breaks and chromosome
1192 asynapsis in mice are monitored by distinct HORMAD2-independent and -dependent
1193 mechanisms. *Genes Dev* **26**:958–973. doi:10.1101/gad.187559.112
1194 Wojtasz L, Daniel K, Roig I, Bolcun-Filas E, Xu H, Boonsanay V, Eckmann CR, Cooke HJ, Jasin M,
1195 Keeney S, McKay MJ, Toth A. 2009. Mouse HORMAD1 and HORMAD2, two conserved
1196 meiotic chromosomal proteins, are depleted from synapsed chromosome axes with the
1197 help of TRIP13 AAA-ATPase. *PLoS Genet* **5**:e1000702. doi:10.1371/journal.pgen.1000702
1198 Xu Y, Qiao H. 2021. A Hypothesis: Linking Phase Separation to Meiotic Sex Chromosome
1199 Inactivation and Sex-Body Formation. *Front Cell Dev Biol* **9**:674203.
1200 doi:10.3389/fcell.2021.674203
1201 Yamane K, Wu X, Chen J. 2002. A DNA damage-regulated BRCT-containing protein, TopBP1, is
1202 required for cell survival. *Mol Cell Biol* **22**:555–566. doi:10.1128/MCB.22.2.555-566.2002
1203 Yeo AJ, Becherel OJ, Luff JE, Graham ME, Richard D, Lavin MF. 2015. Senataxin controls meiotic
1204 silencing through ATR activation and chromatin remodeling. *Cell Discovery* **1**.
1205 doi:10.1038/celldisc.2015.25
1206 Zhou ZW, Liu C, Li TL, Bruhn C, Krueger A, Min WK, Wang ZQ, Carr AM. 2013. An Essential Function
1207 for the ATR-Activation-Domain (AAD) of TopBP1 in Mouse Development and Cellular
1208 Senescence. *PLoS Genet* **9**. doi:10.1371/journal.pgen.1003702
1209

Figure legends

Figure 1. A new TOPBP1 mutant separating its role in fertility from organismal viability.
A) Schematic showing mutations in the *Topbp1 B5* allele. B) Body mass (*Topbp1*$^{+/+}$ Mean = 25.26, SD = 2.38; *Topbp1*$^{B5/B5}$ Mean = 26.43, SD = 2.28, n = 9) and C) appearance of *Topbp1*$^{B5/B5}$ and *Topbp1*$^{+/+}$ littermate mice. D) Effect of full body IR (7 Gy) on changes in body mass of *Topbp1*$^{B5/B5}$ and *Topbp1*$^{+/+}$ littermate mice E) Breeding scheme and resulting litters. F) and G) Comparison of testes size (*Topbp1*$^{+/+}$ Mean = 0.038, SD = 0.006; *Topbp1*$^{B5/B5}$ Mean = 0.011, SD = 0.004, n = 9), and H) sperm count, of *Topbp1*$^{B5/B5}$ and *Topbp1*$^{+/+}$ littermate mice (*Topbp1*$^{+/+}$ Mean = 2.1 x 10^7, SD = 6x 10^6; *Topbp1*$^{B5/B5}$ Mean = 0.0, SD = 0.0, n = 9). I) H&E-stained histological testes sections displaying loss of cellularity in *Topbp1*$^{B5/B5}$. Green arrow = spermatogonia, Red arrow = healthy spermatocyte, Blue arrow = dying spermatocyte. J) and K) TUNEL assay performed on histological testes sections (*Topbp1*$^{+/+}$ Mean = 0.36, SD = 0.15; *Topbp1*$^{B5/B5}$ Mean = 4.80, SD = 0.43, n = 3). L) Meiotic spreads stained for SYCP3, SYCP1 and H1t. **** = p< 0.0001, n = number of mice. p-Values were calculated using unpaired *t*-test.

Figure 2. *Topbp1*$^{B5/B5}$ MEFs display no detectable DDR defects.
A) MEFs obtained from littermate mice of indicated genotypes were subjected to clonogenic survival assay in the indicated concentrations of hydroxyurea, or C) phleomycin. B) and D) Quantification of clonogenic survival assays from A and C, respectively, performed in biological and experimental triplicates. D) Western blot for indicated DDR markers in MEFs obtained from *Topbp1*$^{B5/B5}$ and *Topbp1*$^{+/+}$ littermate mice. The data from MEFs were performed using littermate pairs and validated using a second pair of *Topbp1*$^{B5/B5}$ and *Topbp1*$^{+/+}$ littermate mice. E) Immunofluorescence of MDC1 and phosphoH2AX_S139-stained nuclei from *Topbp1*$^{B5/B5}$ and *Topbp1*$^{+/+}$ MEFs treated with IR (7 Gy).

Figure 3. Markers of DNA repair, synapsis, sex body formation and TOPBP1 localization are mostly normal in *Topbp1*$^{B5/B5}$ spermatocytes.
A) Meiotic spreads showing *Topbp1*$^{+/+}$ and *Topbp1*$^{B5/B5}$ spermatocytes stained with SYCP3 and γH2AX, prepared as described in methods. B) Quantification of γH2AX-stained pachytene spreads, upper graph XY body (each dot represents one pachytene cell measured; *Topbp1*$^{+/+}$ number of cells = 386, number of mice = 8; *Topbp1*$^{B5/B5}$ number of cells = 410, number of mice = 8; p-value = 0.3063), bottom graph autosomal chromosomes (each dot represents the average of signal from all autosomes in each mouse, *Topbp1*$^{+/+}$ number of cells = 160, number of mice = 8; *Topbp1*$^{B5/B5}$ number of cells = 161, number of mice = 8; p-value = 0.5081. C) Meiotic spreads showing *Topbp1*$^{+/+}$ and *Topbp1*$^{B5/B5}$ pachytene spermatocytes stained with SYCP3 and RAD51. D) Quantification of RAD51 foci/cell of mid-pachytene meiotic spreads (each

dot represents one pachytene cell measured; *Topbp1*$^{+/+}$ number of cells = 149, number of mice = 3; *Topbp1*$^{B5/B5}$ number of cells = 183, number of mice = 3; p-value = 0.2174). E) Meiotic spreads showing *Topbp1*$^{+/+}$ and *Topbp1*$^{B5/B5}$ pachytene spermatocytes stained with SYCP3 and SYCP1. F) Meiotic spreads showing *Topbp1*$^{+/+}$ and *Topbp1*$^{B5/B5}$ pachytene spermatocytes stained with SYCP3 and TOPBP1. G) Quantification of TOPBP1 on X and Y chromosome cores from F (each dot represents one pachytene cell measured; *Topbp1*$^{+/+}$ number of cells = 246, number of mice = 3; *Topbp1*$^{B5/B5}$ number of cells = 233, number of mice = 3; p-value = 0.8546). H) Quantification of TOPBP1 on X and Y chromatin loops from F (each dot represents one pachytene cell measured; *Topbp1*$^{+/+}$ number of cells = 246, number of mice = 3; *Topbp1*$^{B5/B5}$ number of cells = 233, number of mice = 3; p-value = 0.6755). n = number of mice. p-Values were calculated using a linear mixed effect model (see Materials and Methods for details).

Figure 4. *Topbp1*$^{B5/B5}$ spermatocytes display normal localization of ATR, BRCA1, MDC1 and pMDC1-T4.

A) Meiotic spreads showing *Topbp1*$^{+/+}$ and *Topbp1*$^{B5/B5}$ pachytene spermatocytes stained with SYCP3 and ATR. B) Quantification of ATR in pachytene spreads from A. Left: ATR on X and Y chromosome cores (each dot represents one pachytene cell measured; *Topbp1*$^{+/+}$ number of cells = 127, number of mice = 3; *Topbp1*$^{B5/B5}$ number of cells = 127, number of mice = 3; p-value = 0.4068). Right: ATR on X and Y chromatin loops (each dot represents one pachytene cell measured; *Topbp1*$^{+/+}$ number of cells = 127, number of mice = 3; *Topbp1*$^{B5/B5}$ number of cells = 127, number of mice = 3; p-value = 0.9396). C) Meiotic spreads showing *Topbp1*$^{+/+}$ and *Topbp1*$^{B5/B5}$ pachytene spermatocytes stained with SYCP3 and BRCA1. D) Quantification of BRCA1 in pachytene spreads from C (each dot represents one pachytene cell measured; *Topbp1*$^{+/+}$ number of cells = 152, number of mice = 3; *Topbp1*$^{B5/B5}$ number of cells = 140, number of mice = 3; p-value = 0.6509). E) Meiotic spreads showing *Topbp1*$^{+/+}$ and *Topbp1*$^{B5/B5}$ pachytene spermatocytes stained with SYCP3 and MDC1. F) Quantification of MDC1 in pachytene spreads from E (each dot represents one pachytene cell measured; *Topbp1*$^{+/+}$ number of cells = 696, number of mice = 8; *Topbp1*$^{B5/B5}$ number of cells = 988, number of mice = 8; p-value = 0.3603). G) Meiotic spreads showing *Topbp1*$^{+/+}$ and *Topbp1*$^{B5/B5}$ pachytene spermatocytes stained with SYCP3 and pCHK1-S317. H) Quantification of pCHK1-S317 in pachytene spreads from G (each dot represents one pachytene cell measured; *Topbp1*$^{+/+}$ number of cells = 223, number of mice = 3; *Topbp1*$^{B5/B5}$ number of cells = 254, number of mice = 3; **p-value = 0.0023). p-Values were calculated using a linear mixed effect model (see Materials and Methods for details). I) Table summarizing the normal or disrupted ATR and TOPBP1-dependent events during male fertility accessed in *Topbp1*$^{B5/B5}$. n = number of mice.

Figure 5. Defective SETX phosphorylation and localization in *Topbp1*$^{B5/B5}$ spermatocytes.

A) Scatter plot of phosphoproteomic datasets corresponding to *Topbp1*$^{+/+}$/*Topbp1*$^{B5/B}$ (Y axis) and *Topbp1*$^{+/+}$(vehicle)/*Topbp1*$^{+/+}$(AZ20) (X axis) from whole testes of mice. B) SETX phosphopeptides identified in the *Topbp1*$^{+/+}$/*Topbp1*$^{B5/B}$ phosphoproteomic experiment shown in A. Red: reduced in *Topbp1*$^{B5/B}$ mutant; Blue: unchanged. C) Meiotic spreads showing pachytene spermatocytes from *Topbp1*$^{+/+}$ and *Topbp1*$^{B5/B5}$ mice stained with SYCP3 and SETX in regular immunofluorescence. D) 3D-SIM analysis of meiotic spreads described in C. E) Quantification of SETX on X and Y chromatin loops in pachytene spreads from C (each dot represents one pachytene cell measured; *Topbp1*$^{+/+}$ number of cells = 152, number of mice = 4; *Topbp1*$^{B5/B5}$ number of cells = 174, number of mice = 4; *p-value = 0.0452). F) Quantification of SETX on X and Y chromosome cores in pachytene spreads from C (each dot represents one pachytene cell measured; *Topbp1*$^{+/+}$ number of cells = 152, number of mice = 4; *Topbp1*$^{B5/B5}$ number of cells = 174, number of mice = 4; p-value = 0.5987). p-Values were calculated using a linear mixed effect model (see Materials and Methods for details).

Figure 6. Single cell RNAseq reveals that *Topbp1*$^{B5/B5}$ spermatocytes initiate MSCI but fail to promote full silencing.

A) scRNAseq workflow for isolation and purification of single cells for RNA-seq. B) UMAP analysis of sub-clusters captured in the scRNAseq, representing all cells captured for both, *Topbp1*$^{+/+}$ and *Topbp1*$^{B5/B5}$. C) UMAP analysis of sub-clusters captured in the scRNAseq of *Topbp1*$^{+/+}$. D) UMAP analysis of sub-clusters captured in the scRNAseq of *Topbp1*$^{+/+}$ (gray) and *Topbp1*$^{B5/B5}$ (blue). E) Violin plots displaying the ratio of the average expression of X chromosome genes by the average expression of chromosome 9 genes at different stages of spermatogenesis for *Topbp1*$^{+/+}$ and *Topbp1*$^{B5/B5}$ cells. The level of X-genes expression in Spermatocyte 3 is significantly higher in *Topbp1*$^{B5/B5}$ cells when compared to *Topbp1*$^{+/+}$ cells, with a p-value of 1.5e-178 using a two-sided Wilcoxon rank sum test.

Figure 7. Topbp1 regulates silencing dynamics of X genes at the Spermatocyte 3 stage.

A) Illustration of the gene markers used to define spermatocyte 1 as leptotene, spermatocyte 2 as zygotene, and spermatocyte 3 as pachytene; hypothetical examples illustrating the categorization of transitions in silencing dynamics between the stages of pre-leptotene (PL), spermatocyte 1 (SP1), spermatocyte 2 (SP2), spermatocyte 3 (SP3). B) Number of genes in each of the categories described in A, during the different stage transitions and respective p-values above each graph (the p-values were calculated using the Fisher's exact test). C) Examples of genes with altered silencing dynamics in the *Topbp1*$^{B5/B5}$, red = reduced silencing, blue = unaltered silencing and green = increased silencing D) Scatter plot showing the difference in RNA level between *Topbp1*$^{+/+}$ and *Topbp1*$^{B5/B5}$ for each of the indicated stage transitions. E) Scatter plot showing expression level of X-chromosome genes, normalized to pre-leptotene levels, in *Topbp1*$^{+/+}$ (gray)

and *Topbp1*$^{B5/B5}$ (blue) at SP3. F) Graph plotting expression levels of X-chromosome genes, normalized to pre-leptotene levels, in *Topbp1*$^{+/+}$ (Y axis) and *Topbp1*$^{B5/B5}$ (X axis) and split in three categories based on the severity of silencing defect. G) Box plot showing PL expression levels of X-chromosome genes in each of the categories of silencing defect severity shown in F.

Figure 8. A new TOPBP1 mutant separates XY silencing from sex body formation.

Schematic of sub-stages of meiotic prophase I. In Wild-type mice, MSCI initiates following the accumulation of the DDR proteins at the XY chromosomes. During mid-pachytene, the XY body is fully formed, and transcription is restricted to the autosomes. In *Atr* or *Topbp1* CKOs, the sex body is not formed, and the DDR proteins are not sequestered to the XY. Asynapsis events and transcription of toxic genes at the sex chromosomes are observed, triggering mid-pachytene arrest. In *Topbp1*$^{B5/B5}$, MSCI initiates, the sex body is normally formed with normal recruitment of DDR proteins to the X and Y chromosomes, yet cells fail in the reinforcement/maintenance of silencing. Cells progress through mid-pachytene but not into diplotene.

Supplemental material

Supplemental Figure legends

Supplemental Figure 1. Genotyping of *Topbp1*$^{B5/B5}$ mice.

Sanger sequencing confirms the eight charge reversal point mutations on the BRCT 5 domain of TOPBP1 from homozygous *Topbp1*$^{B5/B5}$ mice.

Supplemental Figure 2. Survival assays of *Topbp1*$^{B5/B5}$ MEFs.

A) MEFs obtained from littermate mice (second independent litter) of indicated genotypes were subjected to clonogenic survival assay in the indicated concentrations of hydroxyurea, or B) phleomycin.

Supplemental Figure 3. Absence of an increased number of micronuclei in *Topbp1*$^{B5/B5}$ MEFs.

Immunofluorescence showing DAPI-stained nuclei and micronuclei quantification of *Topbp1*$^{+/+}$ and *Topbp1*$^{B5/B5}$ A) MEFs #1 and B) MEFs #2. (MEFs #2 is a second independent litter).

Supplemental Figure 4. TOPBP1-B5 shows disruption in binding 53BP1 and BLM.

A) HEK-293T cells were transfected with plasmids expressing wild-type TOPBP1 or indicated BRCT mutants (K155A - BRCT 1, K250A - BRCT 2, K704A - BRCT 5, K1713A - BRCT 7, and B5 - 8 mutations in BRCT 5), with a 3xFlag tag. After cell lysis and anti-Flag IP, lysate and elution were analyzed by western blot for the indicated proteins. B) IP-mass spectrometry of flagTOPBP1 wild type versus flag-TOPBP1-B5 was performed in silac-labeled HEK-293T cells. Cell transfections, lysis, protein IP, and elution were performed as described in A. From left to right, the TOPBP1 interactors were plotted from highest to lowest binding. The size of circles represents the number of peptide hits.

Supplemental Figure 5. *Topbp1*$^{B5/B5}$ MEFs show lower TOPBP1 protein abundance than *Topbp1* $^{+/+}$ MEFs.

Western blot probing TOPBP1 in MEFs, *Topbp1* $^{+/+}$, *Topbp1*$^{B5/+}$, and *Topbp1*$^{B5/B5}$ in two biological replicates.

Supplemental Figure 6. *Topbp1*$^{B5/B5}$ mid-pachytene spermatocytes show normal HORMAD1, HORMAD2, pHORMAD1 and pCHK1_S345 localization and intensities.

A) *Topbp1*$^{+/+}$ and *Topbp1*$^{B5/B5}$ pachytene spermatocytes stained with HORMAD1 and SYCP3, prepared as described in methods. B) *Topbp1*$^{+/+}$ and *Topbp1*$^{B5/B5}$ pachytene spermatocytes stained with HORMAD2

and SYCP3. C) Meiotic spreads showing *Topbp1*$^{+/+}$ and *Topbp1*$^{B5/B5}$ pachytene spermatocytes stained with SYCP3 and pMDC1-T4 prepared as described in methods. D) Quantification of pMDC1-T4-stained pachytene spreads from C (each dot represents one pachytene cell measured; *Topbp1*$^{+/+}$ number of cells = 60, number of mice = 3; *Topbp1*$^{B5/B5}$ number of cells = 159, number of mice = 3; p-value = 0.8193). E) Meiotic spreads showing *Topbp1*$^{+/+}$ and *Topbp1*$^{B5/B5}$ pachytene spermatocytes stained with SYCP3 and pCHK1-S345. F) Quantification of pCHK1-S345-stained pachytene spreads from E (each dot represents one pachytene cell measured; *Topbp1*$^{+/+}$ number of cells = 168, number of mice = 2; *Topbp1*$^{B5/B5}$ number of cells = 125, number of mice = 2; p-value =0.6536). G) Meiotic spreads showing *Topbp1*$^{+/+}$ and *Topbp1*$^{B5/B5}$ pachytene spermatocytes stained with SYCP3 and pHORMAD1-S271. H) Quantification of pHORMAD1-S271-stained pachytene spreads from G (each dot represents one pachytene cell measured; *Topbp1*$^{+/+}$ number of cells = 224, number of mice = 3; *Topbp1*$^{B5/B5}$ number of cells = 254, number of mice = 3; p-value =0.2811). p-Values were calculated using a linear mixed effect model (see Materials and Methods for details).

Supplemental Figure 7. *Topbp1*$^{B5/B5}$ mid-pachytene spermatocytes show an increased number of MLH1 foci/cell but no difference in the number of MHL3 foci/cell.

A) Meiotic spreads showing *Topbp1*$^{+/+}$ and *Topbp1*$^{B5/B5}$ pachytene spermatocytes stained with SYCP3 and MLH1, prepared as described in methods. B) Foci count of MLH1-stained pachytene spreads from A (each dot represents the number of foci/cell; *Topbp1*$^{+/+}$ number of cells = 84, number of mice = 4; *Topbp1*$^{B5/B5}$ number of cells = 94, number of mice = 4; p-value < 0.0001). C) Meiotic spreads showing *Topbp1*$^{+/+}$ and *Topbp1*$^{B5/B5}$ pachytene spermatocytes stained with SYCP3 and MLH3 prepared as described in methods. D) Foci count of MLH3-stained pachytene spreads from C (each dot represents the number of foci/cell; *Topbp1*$^{+/+}$ number of cells = 48, number of mice = 3; *Topbp1*$^{B5/B5}$ number of cells = 91, number of mice = 3; p-value = 0.4088). p-Values were calculated using a linear mixed effect model (see Materials and Methods for details).

Supplemental Figure 8. *Topbp1*$^{B5/B5}$ mid-pachytene spermatocytes form a normal sex body.

Topbp1$^{+/+}$ and *Topbp1*$^{B5/B5}$ mid-pachytene spermatocytes stained with DAPI and SYCP3, prepared as described in methods.

Supplemental Figure 9. *Topbp1*$^{B5/B5}$ mid-pachytene spermatocytes show subtle defects/delays in the spreading of γH2AX on XY chromosomes.

Quantification and representative images of *Topbp1*$^{B5/B5}$ mid-pachytene spermatocytes showing: A) normal spreading of γH2AX on XY chromosomes; B) defect/delay in the spreading of γH2AX at the PAR; C)

defect/delay in the spreading of γH2AX at the pericentromeric region of the Y chromosome; D) spreading of γH2AX into an autosomal chromosome fused to the X chromosome; and E) other types of defects/delays in the spreading of γH2AX onto the XY chromosomes. Each dot in the graph represents the sum of the cells counted per mouse. F) Percentage of the previously described defects found in *Topbp1*$^{+/+}$ or G) *Topbp1*$^{B5/B5}$ mid-pachytene spermatocytes. *p < 0.05, **p < 0.01, ***p < 0.001, and **** p < 0.0001. p-Values were calculated using unpaired *t*-test in GraphPad. n = number of mice.

Supplemental Figure 10. TOPBP1 is normally localized in all stages of prophase I in *Topbp1*$^{B5/B5}$.
Meiotic spreads showing *Topbp1*$^{+/+}$ and *Topbp1*$^{B5/B5}$ spermatocytes stained with SYCP3 and TOPBP1, prepared as described in methods.

Supplemental Figure 11. 53BP1 localization in *Topbp1*$^{B5/B5}$ mid-pachytene spermatocytes.
Representative images of meiotic spreads showing *Topbp1*$^{+/+}$ and *Topbp1*$^{B5/B5}$ pachytene spermatocytes stained with SYCP3 and 53BP1 on the left, and quantification of 53BP1-stained pachytene spreads on the right (each dot represents one pachytene cell measured; *Topbp1*$^{+/+}$ number of cells = 95, number of mice = 2; *Topbp1*$^{B5/B5}$ number of cells = 171, number of mice = 2; p-value = 0.2384). p-Values were calculated using a linear mixed effect model (see Materials and Methods for details).

Supplemental Figure 12. *Topbp1*$^{B5/B5}$ pachytene spermatocytes do not exhibit any difference in CHD4, Sumo2-3, and USP7 intensities and localization compared to *Topbp1*$^{+/+}$.
A) Representative images of meiotic spreads showing *Topbp1*$^{+/+}$ and *Topbp1*$^{B5/B5}$ pachytene spermatocytes stained with SYCP3 and CHD4 on the left, and quantification of CHD4-stained pachytene spreads on the right (each dot represents one pachytene cell measured; *Topbp1*$^{+/+}$ number of cells = 176, number of mice = 4; *Topbp1*$^{B5/B5}$ number of cells = 215, number of mice = 4; p-value = 0.2125). B) Representative images of meiotic spreads showing *Topbp1*$^{+/+}$ and *Topbp1*$^{B5/B5}$ pachytene spermatocytes stained with SYCP3 and SUMO2.3 on the left, and quantification of SUMO2.3-stained pachytene spreads on the right (each dot represents one pachytene cell measured; *Topbp1*$^{+/+}$ number of cells = 155, number of mice = 2; *Topbp1*$^{B5/B5}$ number of cells = 126, number of mice = 2; p-value = 0.8951). C) Representative images of meiotic spreads showing *Topbp1*$^{+/+}$ and *Topbp1*$^{B5/B5}$ pachytene spermatocytes stained with SYCP3 and USP7 on the left, and quantification of USP7-stained pachytene spreads on the right (each dot represents one pachytene cell measured; *Topbp1*$^{+/+}$ number of cells = 73, number of mice = 2; *Topbp1*$^{B5/B5}$ number of cells = 48, number of mice = 2; p-value = 0.8610). p-Values were calculated using a linear mixed effect model (see Materials and Methods for details).

Supplemental Figure 13. *Topbp1*$^{B5/B5}$ pachytene spermatocytes show no difference in H3K9ac or K3K9me3 staining compared to *Topbp1*$^{+/+}$.

A) Representative images of meiotic spreads showing *Topbp1*$^{+/+}$ and *Topbp1*$^{B5/B5}$ pachytene spermatocytes stained with SYCP3 and H3K9ac on the left, and quantification of H3K9ac-stained pachytene spreads on the right (each dot represents one pachytene cell measured; *Topbp1*$^{+/+}$ number of cells = 214, number of mice = 3; *Topbp1*$^{B5/B5}$ number of cells = 203, number of mice = 3; p-value = 0.4948). B) Representative images of meiotic spreads showing *Topbp1*$^{+/+}$ and *Topbp1*$^{B5/B5}$ pachytene spermatocytes stained with SYCP3 and H3K9me3 on the left, and quantification of H3K9me3-stained pachytene spreads on the right. (Early-pachytene spreads: each dot represents one cell measured; *Topbp1*$^{+/+}$ number of cells = 31, number of mice = 2; *Topbp1*$^{B5/B5}$ number of cells = 48, number of mice = 2; p-value = 0.6374; Mid-pachytene spreads: each dot represents one cell measured; *Topbp1*$^{+/+}$ number of cells = 35, number of mice = 2; *Topbp1*$^{B5/B5}$ number of cells = 86, number of mice = 2; p-value = 0.3990; Late-pachytene: each dot represents one cell measured; *Topbp1*$^{+/+}$ number of cells = 49, number of mice = 2; *Topbp1*$^{B5/B5}$ number of cells = 14, number of mice = 2; p-value = 0.3474). p-Values were calculated using a linear mixed effect model (see Materials and Methods for details).

Supplemental Figure 14. *Topbp1*$^{B5/B5}$ pachytene spermatocytes display no difference in H3K27ac, H3K36me3 or K3K4me3 staining compared to *Topbp1*$^{+/+}$.

A) Representative images of meiotic spreads showing *Topbp1*$^{+/+}$ and *Topbp1*$^{B5/B5}$ pachytene spermatocytes stained with SYCP3 and H3K27ac on the left, and quantification of H3K27ac-stained pachytene spreads on the right (each dot represents one pachytene cell measured; *Topbp1*$^{+/+}$ number of cells = 143, number of mice = 2; *Topbp1*$^{B5/B5}$ number of cells = 56, number of mice = 2; p-value = 0.7881). B) Representative images of meiotic spreads showing *Topbp1*$^{+/+}$ and *Topbp1*$^{B5/B5}$ pachytene spermatocytes stained with SYCP3 and H3K36me3 on the left, and quantification of H3K36me3-stained pachytene spreads on the right (each dot represents one pachytene cell measured; *Topbp1*$^{+/+}$ number of cells = 79, number of mice = 2; *Topbp1*$^{B5/B5}$ number of cells = 52, number of mice = 2; p-value = 0.2778). C) Representative images of meiotic spreads showing *Topbp1*$^{+/+}$ and *Topbp1*$^{B5/B5}$ pachytene spermatocytes stained with SYCP3 and H3K4me3 on the left, and quantification of H3K4me3-stained pachytene spreads on the right. (Early-pachytene spreads: each dot represents one cell measured *Topbp1*$^{+/+}$ number of cells = 7, number of mice = 2; *Topbp1*$^{B5/B5}$ number of cells = 46, number of mice = 2; p-value = 0.9895; Mid-pachytene spreads: each dot represents one cell measured; *Topbp1*$^{+/+}$ number of cells = 26, number of mice = 2; *Topbp1*$^{B5/B5}$ number of cells = 58, number of mice = 2; p-value = 0.3292.). p-Values were calculated using a linear mixed effect model (see Materials and Methods for details).

Supplemental Figure 15. *Topbp1*$^{B5/B5}$ pachytene spermatocytes display no difference in H4K16ac, H4ac or H2AK166ub staining compared to *Topbp1*$^{+/+}$.

A) Representative images of meiotic spreads showing *Topbp1*$^{+/+}$ and *Topbp1*$^{B5/B5}$ pachytene spermatocytes stained with SYCP3 and H4K16ac on the left, and quantification of H4K16ac-stained pachytene spreads, on the right (each dot represents one pachytene cell measured; *Topbp1*$^{+/+}$ number of cells = 19, number of mice = 1; *Topbp1*$^{B5/B5}$ number of cells = 53, number of mice = 2; p-value = 0.7314). B) Representative images of meiotic spreads showing *Topbp1*$^{+/+}$ and *Topbp1*$^{B5/B5}$ pachytene spermatocytes stained with SYCP3 and H4ac on the left, and quantification of H4ac-stained pachytene spreads on the right, (each dot represents one pachytene cell measured; *Topbp1*$^{+/+}$ number of cells = 26, number of mice = 2; *Topbp1*$^{B5/B5}$ number of cells = 87, number of mice = 2; p-value = 0.6795). C) Representative images of meiotic spreads showing *Topbp1*$^{+/+}$ and *Topbp1*$^{B5/B5}$ pachytene spermatocytes stained with SYCP3 and H2A-K199-ub on the left, and quantification of H2A-K199-ub-stained pachytene spreads on the right, (each dot represents one pachytene cell measured; *Topbp1*$^{+/+}$ number of cells = 35, number of mice = 2; *Topbp1*$^{B5/B5}$ number of cells = 20, number of mice = 2; p-value = 0.9941).). p-Values were calculated using a linear mixed effect model (see Materials and Methods for details).

Supplemental Figure 16. From early pachytene to beginning of late pachytene, *Topbp1*$^{B5/B5}$ spermatocytes exhibit the same intensity and localization pattern of H3K4me1 compared to *Topbp1*$^{+/+}$.

Representative images of *Topbp1*$^{+/+}$ and *Topbp1*$^{B5/B5}$ early, mid, and late pachytene spermatocytes stained with H3K4me1 and SYCP3.

Supplemental figure 17. *Topbp1*$^{B5/B5}$ pachytene spermatocytes exhibit no differences in the intensity or localization patterns of RNApol2, pRNApol2_Ser2 or pRNApol2_ser5 compared to *Topbp1*$^{+/+}$.

A) Representative images of meiotic spreads showing *Topbp1*$^{+/+}$ and *Topbp1*$^{B5/B5}$ pachytene spermatocytes stained with SYCP3 and RNApol2 on the left, and quantification of RNApol2-stained pachytene spreads on the right, (each dot represents one pachytene cell measured; *Topbp1*$^{+/+}$ number of cells = 242, number of mice = 6; *Topbp1*$^{B5/B5}$ number of cells = 289, number of mice = 6; p-value for X and Y cores = 0.2026, p-value for X and Y chromatin loops = 0.4407). B) Representative images of meiotic spreads showing *Topbp1*$^{+/+}$ and *Topbp1*$^{B5/B5}$ pachytene spermatocytes stained with SYCP3 and pRNApol2-Ser2 on the left, and quantification of pRNApol2-Ser2-stained pachytene spreads on the right, (each dot represents one pachytene cell measured; *Topbp1*$^{+/+}$ number of cells = 66, number of mice = 5; *Topbp1*$^{B5/B5}$ number of cells = 66, number of mice = 5; p-value = 0.3862). C) Representative images of meiotic spreads showing *Topbp1*$^{+/+}$ and *Topbp1*$^{B5/B5}$ pachytene spermatocytes stained with SYCP3 and pRNApol2-Ser5 on the left,

and quantification of pRNApol2-Ser5-stained pachytene spreads on the right (each dot represents one pachytene cell measured; *Topbp1*$^{+/+}$ number of cells = 47, number of mice = 3; *Topbp1*$^{B5/B5}$ number of cells = 21, number of mice = 2; p-value = 0.5104). p-Values were calculated in GraphPad using a linear mixed effect model. p-Values were calculated using a linear mixed effect model (see Materials and Methods for details).

Supplemental Figure 18. Genes used as markers to define the stages of the germ cells in the scRNAseq analysis.

UMAP plots showing markers for Spermatogonia (*Sal1* and *Dmrt1*), Spermatocytes (*Dazl*, *Id4*, *Sycp3*, and *Shcbp1l*), and Spermatids (*Acrv1*, *Oaz3* and *Prm2*).

Supplemental Figure 19. Genes used as markers to track spermatogenesis progression and form the 47 sub-cluster for all cells captured in the 10X platform in the scRNAseq analysis.

Bubble plot displaying gene markers and their respective pattern of expression during spermatogenesis.

Supplemental Figure 20. Genes used as markers of somatic cells captured in the scRNAseq analysis.

UMAP plots show markers for the somatic cells captured on the germ cell-enriched population, Endothelial and Hematopoietic (*Col1a2*, *Vcam1*, *Laptm5* and *Insl3*), Smooth muscle (*Acta2*) and Sertoli (*Ptgds* and *Wt1*).

Supplemental Figure 21. Analysis of sub-clusters of all cells captured in the 10X platform.

UMAP plot displaying the 47 sub-clusters of cells captured in the scRNAseq analysis.

Supplemental Figure 22. Analysis of the main 24 sub-clusters captured in the germ cells-enriched scRNAseq analysis.

UMAP plot showing 24 sub-clusters for spermatogonia, spermatocytes, round spermatids, spermatids, Sertoli, smooth muscle and endothelial and hematopoietic cells captured in the 10X platform.

Supplemental Figure 23. Spermatocytes from *Topbp1*$^{+/+}$ and *Topbp1*$^{B5/B5}$ show correlation greater than 0.9.

Plot of Pearson correlation values between cell groups separated by cluster and genotype using log-normalized average expression of all genes.

Supplemental Figure 24. *Topbp1*$^{B5/B5}$ pachytene spermatocytes show increased expression of X-linked genes.

Heatmap displaying the expression levels of X-chromosome genes in spermatocyte 3 stage (pachytene) of *Topbp1*$^{B5/B5}$ on the right and *Topbp1*$^{+/+}$ on the left. Each line represents a gene, and each row is a cell.

Supplemental Figure 25. *Topbp1*$^{B5/B5}$ pachytene spermatocytes show increased expression of XY "killer genes" and other X and Y genes typically used to illustrate MSCI defects.

Violin plots showing the level of expression and number of cells expressing the XY chromosome genes in SP3 (pachytene): *Zfy1*, *Zfy2*, *Kdm6a*, *Lamp2*, *Scml2*, *Zfx*, *Uba1y* and *Rhox13* in *Topbp1*$^{B5/B5}$ and in *Topbp1*$^{+/+}$. The Wilcoxon test was used to calculate the p-values. **p < 0.01, ***p < 0.001, and **** p < 0.0001.

Supplemental Figure 26. *Topbp1*$^{B5/B5}$ pachytene spermatocytes show increased expression of XY-linked genes.

Bar plots showing the number of cells expressing the XY chromosome genes in SP3 (pachytene): *Zfy1*, *Zfy2*, *Kdm6a*, *Lamp2*, *Scml2*, *Zfx*, *Uba1y* and *Rhox13* in *Topbp1*$^{B5/B5}$ and in *Topbp1*$^{+/+}$. Fisher's exact test was used to calculate the p-values. **p < 0.01, ***p < 0.001, and **** p < 0.0001.

Supplemental Figure 27. Analysis of the gene marker used to define the zygotene stage.

UMAP analysis of the gene *Gm960* was used as a gene marker to define the zygotene stage.

Supplemental Figure 28. Expression levels of genes with no defects, mild defects, and strong defects in *Topbp1*$^{B5/B5}$ and *Topbp1*$^{+/+}$.

Boxplot showing the expression levels of the clusters of genes with no defects, mild defects, and strong defects from pre-leptotene to Spermatocyte 3 (pachytene) in *Topbp1*$^{B5/B5}$ and *Topbp1*$^{+/+}$. The Wilcoxon rank-sum test was used to calculate the p-values. *p < 0.05, **p < 0.01, ***p < 0.001, and **** p < 0.0001.

Supplemental Figure 29. Quality control of the scRNAseq data.

Violin plots show the quality control for the scRNAseq data, displaying the distribution of gene counts, UMI counts, and mitochondrial gene percentage per library before filtering data.

Figure 1

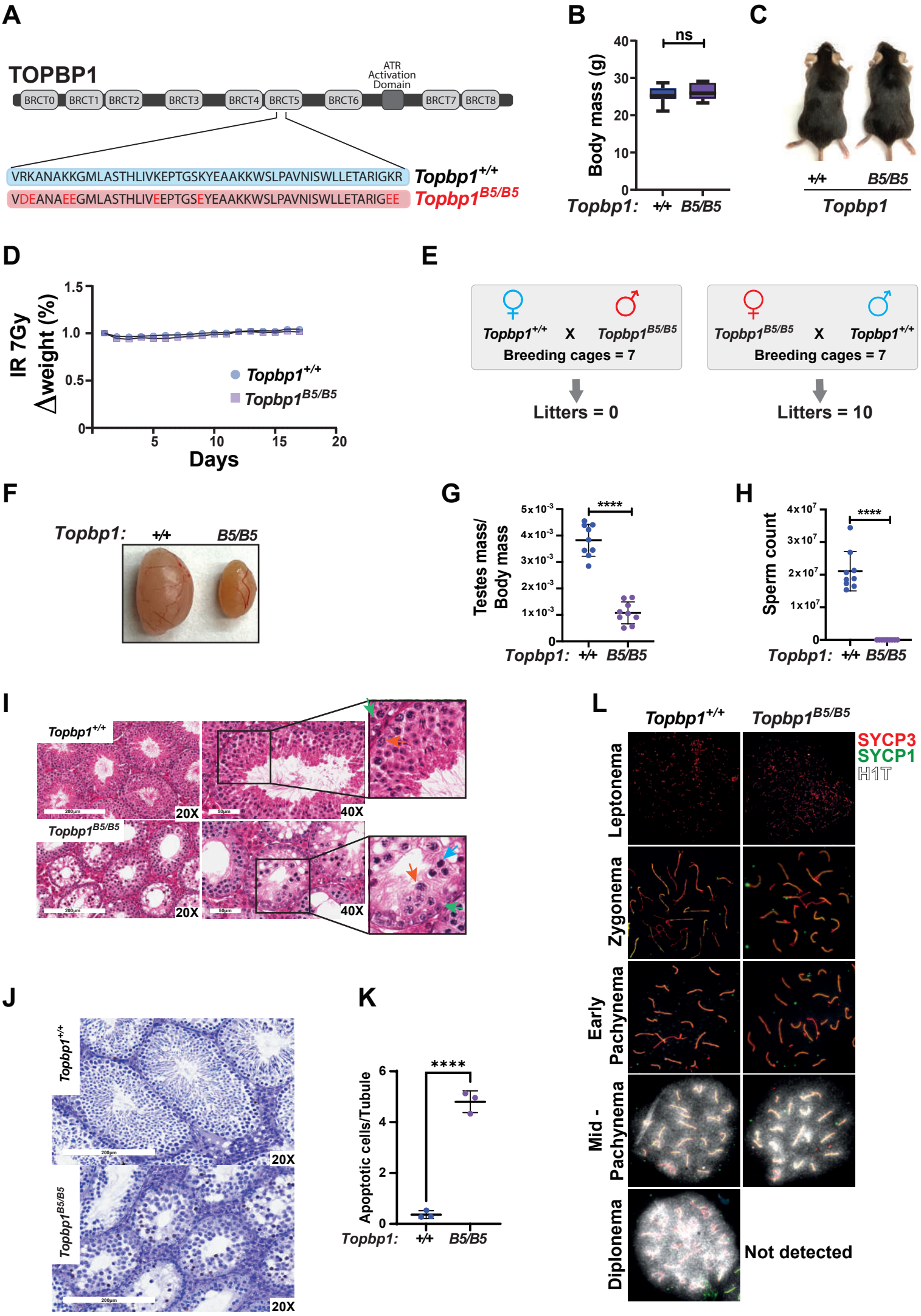
A
TOPBP1
ATR Activation Domain
BRCT0
BRCT1
BRCT2
BRCT3
BRCT4
BRCT5
BRCT6
BRCT7
BRCT8
VRKANAKKGMLASTHLIVKEPTGSKYEAAKKWSLPAVNISWLLETARIGKR
Topbp1+/+
VDEANAEEGMLASTHLIVEEPTGSEYEAAKKWSLPAVNISWLLETARIGEE
Topbp1B5/B5
B
ns
Body mass (g)
Topbp1: +/+ B5/B5
C
+/+
B5/B5
Topbp1
D
IR 7Gy
Δweight (%)
Topbp1+/+
Topbp1B5/B5
Days
E
Topbp1+/+ X Topbp1B5/B5
Breeding cages = 7
Litters = 0
Topbp1B5/B5 X Topbp1+/+
Breeding cages = 7
Litters = 10
F
Topbp1: +/+ B5/B5
G
Testes mass/ Body mass
****
Topbp1: +/+ B5/B5
H
Sperm count
****
Topbp1: +/+ B5/B5
I
Topbp1+/+
Topbp1B5/B5
20X
40X
J
Topbp1+/+
Topbp1B5/B5
20X
K
Apoptotic cells/Tubule
****
Topbp1: +/+ B5/B5
L
Topbp1+/+
Topbp1B5/B5
SYCP3
SYCP1
H1T
Leptonema
Zygonema
Early Pachynema
Mid - Pachynema
Diplonema
Not detected

Figure 2

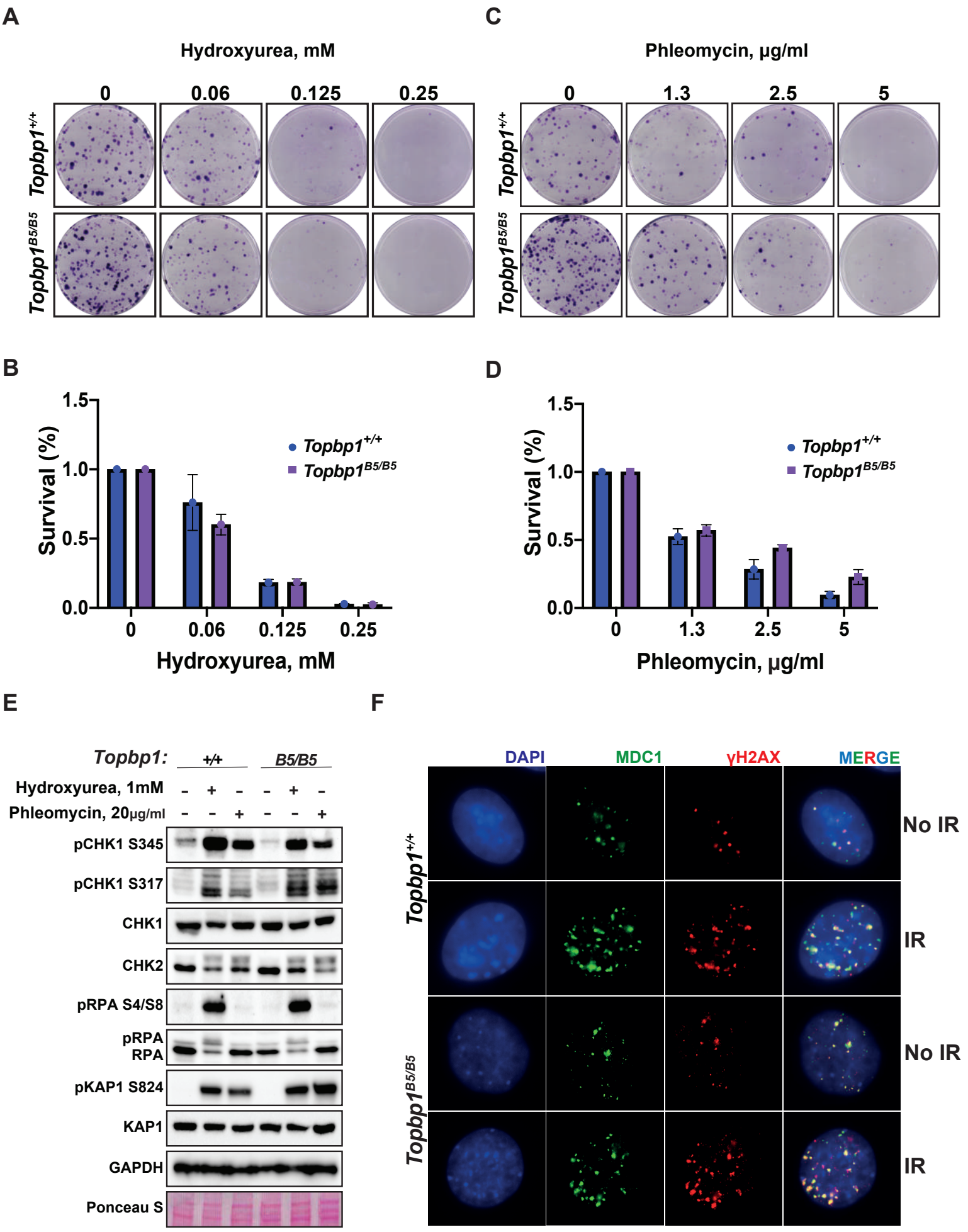
A
Hydroxyurea, mM
0
0.06
0.125
0.25
Topbp1+/+
Topbp1B5/B5
C
Phleomycin, µg/ml
0
1.3
2.5
5
Topbp1+/+
Topbp1B5/B5
B
Survival (%)
1.5
1.0
0.5
0.0
Topbp1+/+
Topbp1B5/B5
0
0.06
0.125
0.25
Hydroxyurea, mM
D
Survival (%)
1.5
1.0
0.5
0.0
Topbp1+/+
Topbp1B5/B5
0
1.3
2.5
5
Phleomycin, µg/ml
E
Topbp1:
+/+
B5/B5
Hydroxyurea, 1mM
Phleomycin, 20µg/ml
pCHK1 S345
pCHK1 S317
CHK1
CHK2
pRPA S4/S8
pRPA
RPA
pKAP1 S824
KAP1
GAPDH
Ponceau S
F
DAPI
MDC1
γH2AX
MERGE
Topbp1+/+
Topbp1B5/B5
No IR
IR
No IR
IR

Figure 3

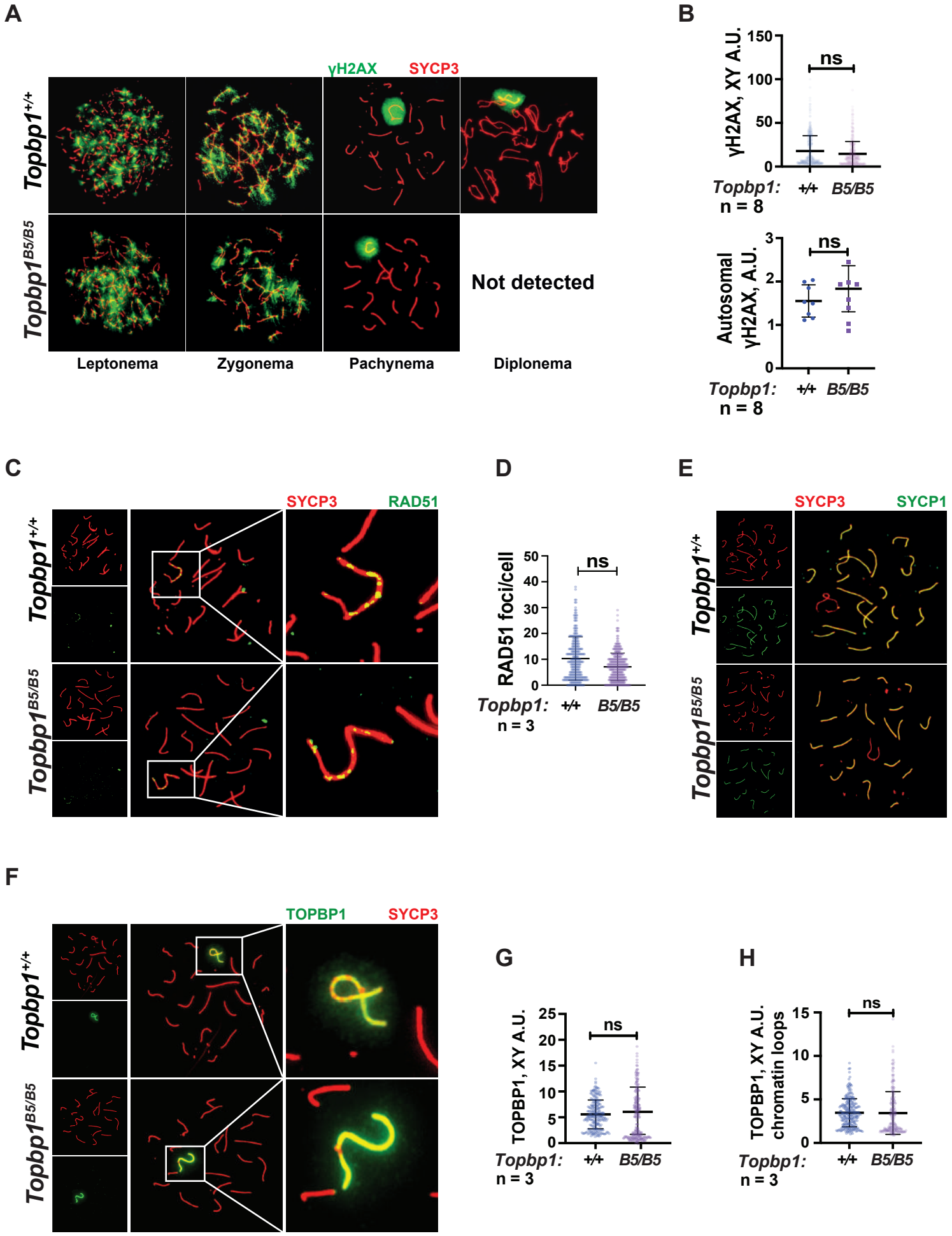
A
γH2AX
SYCP3
Topbp1+/+
Topbp1B5/B5
Not detected
Leptonema
Zygonema
Pachynema
Diplonema
B
γH2AX, XY A.U.
150
100
50
0
ns
Topbp1: +/+ B5/B5
n = 8
Autosomal γH2AX, A.U.
3
2
1
0
ns
Topbp1: +/+ B5/B5
n = 8
C
SYCP3
RAD51
Topbp1+/+
Topbp1B5/B5
D
RAD51 foci/cell
50
40
30
20
10
0
ns
Topbp1: +/+ B5/B5
n = 3
E
SYCP3
SYCP1
Topbp1+/+
Topbp1B5/B5
F
TOPBP1
SYCP3
Topbp1+/+
Topbp1B5/B5
G
TOPBP1, XY A.U.
25
20
15
10
5
0
ns
Topbp1: +/+ B5/B5
n = 3
H
TOPBP1, XY A.U. chromatin loops
15
10
5
0
ns
Topbp1: +/+ B5/B5
n = 3

Figure 4

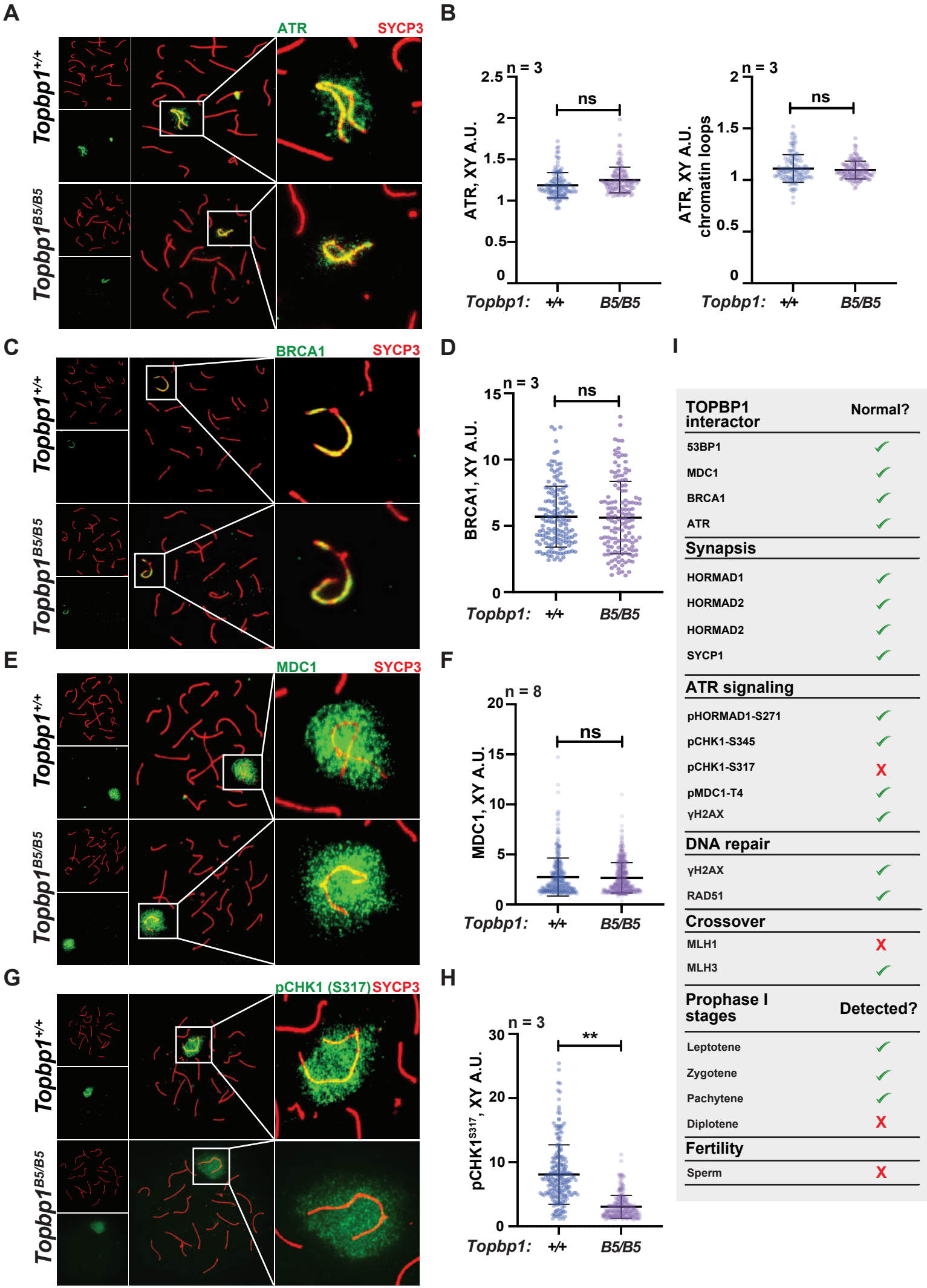
A
ATR
SYCP3
Topbp1+/+
Topbp1B5/B5
B
n = 3
ns
ATR, XY A.U.
2.5
2
1.5
1
0.5
0
Topbp1: +/+ B5/B5
n = 3
ns
ATR, XY A.U. chromatin loops
2
1.5
1
0.5
0
Topbp1: +/+ B5/B5
C
BRCA1
SYCP3
Topbp1+/+
Topbp1B5/B5
D
n = 3
ns
BRCA1, XY A.U.
15
10
5
0
Topbp1: +/+ B5/B5
I
TOPBP1 interactor | Normal?
53BP1 ✓
MDC1 ✓
BRCA1 ✓
ATR ✓
Synapsis
HORMAD1 ✓
HORMAD2 ✓
HORMAD2 ✓
SYCP1 ✓
ATR signaling
pHORMAD1-S271 ✓
pCHK1-S345 ✓
pCHK1-S317 X
pMDC1-T4 ✓
γH2AX ✓
DNA repair
γH2AX ✓
RAD51 ✓
Crossover
MLH1 X
MLH3 ✓
Prophase I stages | Detected?
Leptotene ✓
Zygotene ✓
Pachytene ✓
Diplotene X
Fertility
Sperm X
E
MDC1
SYCP3
Topbp1+/+
Topbp1B5/B5
F
n = 8
ns
MDC1, XY A.U.
20
15
10
5
0
Topbp1: +/+ B5/B5
G
pCHK1 (S317)
SYCP3
Topbp1+/+
Topbp1B5/B5
H
n = 3
**
pCHK1S317, XY A.U.
30
20
10
0
Topbp1: +/+ B5/B5

Figure 5

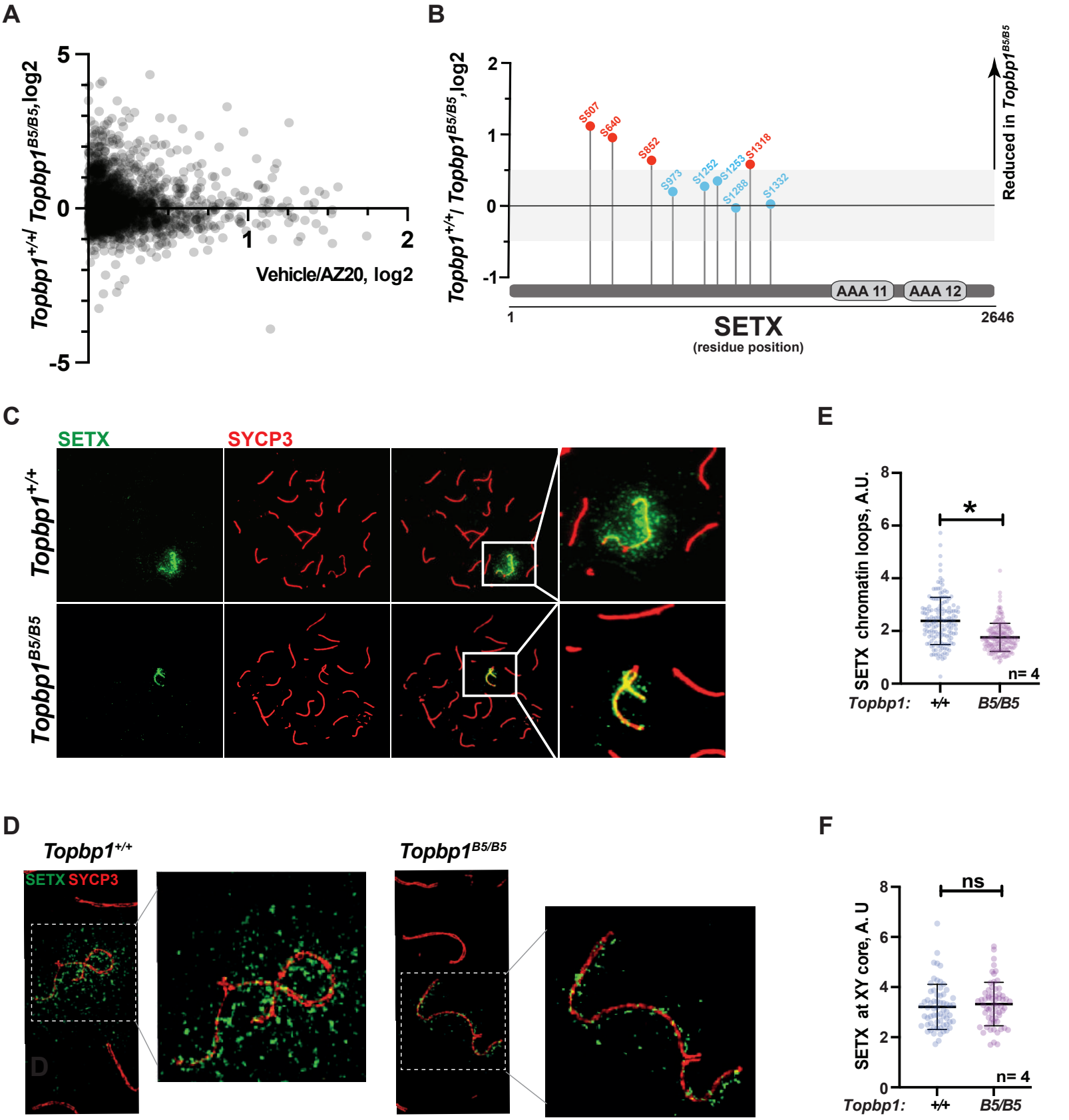
A
Topbp1+/+/ Topbp1B5/B5,log2
Vehicle/AZ20, log2
B
Topbp1+/+/ Topbp1B5/B5,log2
Reduced in Topbp1B5/B5
S507
S640
S852
S973
S1252
S1253
S1318
S1288
S1332
AAA 11
AAA 12
SETX
(residue position)
C
SETX
SYCP3
Topbp1+/+
Topbp1B5/B5
E
SETX chromatin loops, A.U.
n= 4
Topbp1:
+/+
B5/B5
D
Topbp1+/+
Topbp1B5/B5
SETX SYCP3
F
SETX at XY core, A. U
ns
n= 4
Topbp1:
+/+
B5/B5

Figure 6

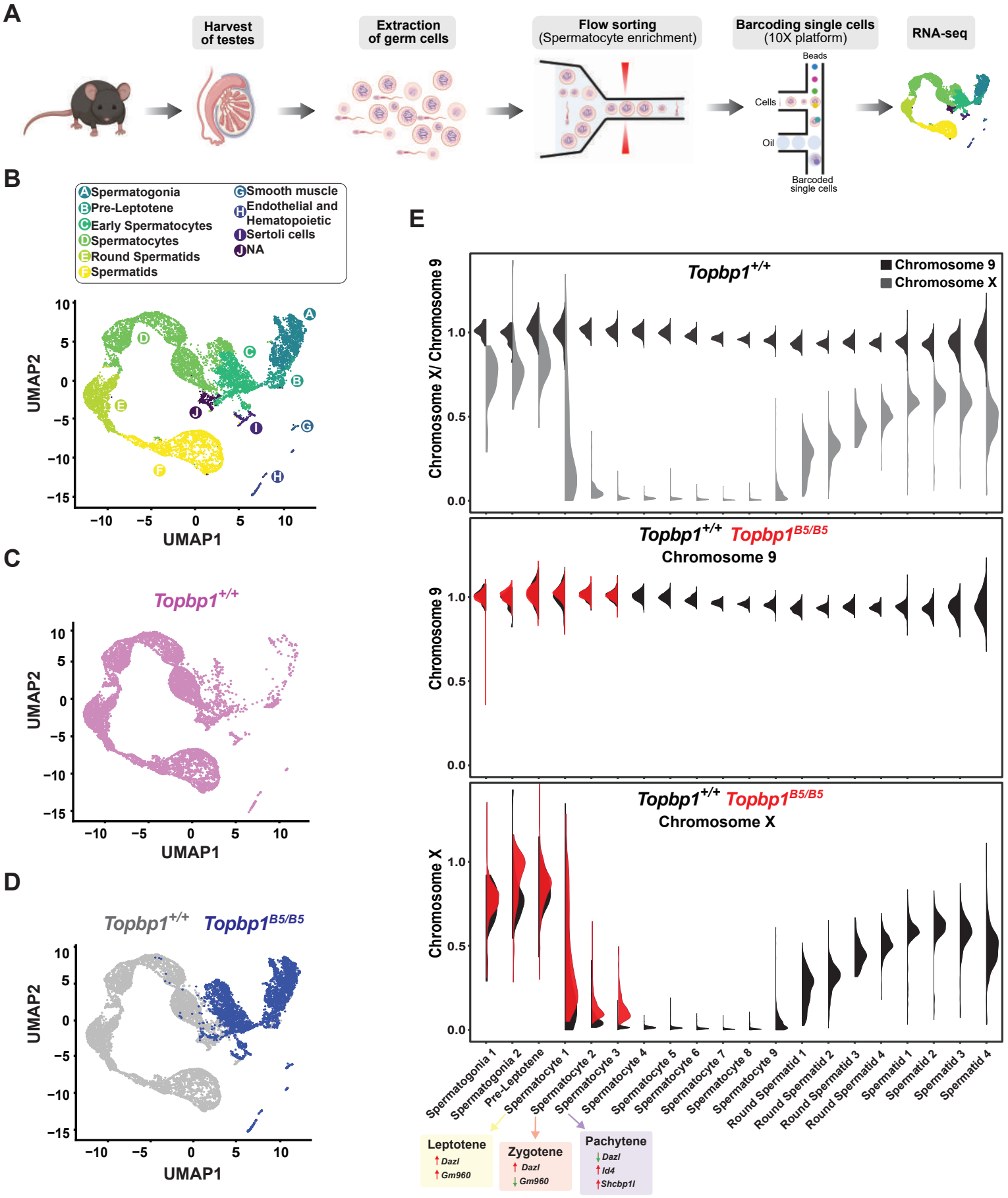
A
Harvest of testes
Extraction of germ cells
Flow sorting (Spermatocyte enrichment)
Barcoding single cells (10X platform)
RNA-seq
Beads
Cells
Oil
Barcoded single cells
B
A Spermatogonia
B Pre-Leptotene
C Early Spermatocytes
D Spermatocytes
E Round Spermatids
F Spermatids
G Smooth muscle
H Endothelial and Hematopoietic
I Sertoli cells
J NA
UMAP2
UMAP1
C
Topbp1+/+
D
Topbp1+/+ Topbp1B5/B5
E
Topbp1+/+
Chromosome 9
Chromosome X
Chromosome X/ Chromosome 9
Topbp1+/+ Topbp1B5/B5
Chromosome 9
Topbp1+/+ Topbp1B5/B5
Chromosome X
Spermatogonia 1
Spermatogonia 2
Pre-Leptotene
Spermatocyte 1
Spermatocyte 2
Spermatocyte 3
Spermatocyte 4
Spermatocyte 5
Spermatocyte 6
Spermatocyte 7
Spermatocyte 8
Spermatocyte 9
Round Spermatid 1
Round Spermatid 2
Round Spermatid 3
Round Spermatid 4
Spermatid 1
Spermatid 2
Spermatid 3
Spermatid 4
Leptotene
Dazl
Gm960
Zygotene
Dazl
Gm960
Pachytene
Dazl
Id4
Shcbp1l

Figure 7

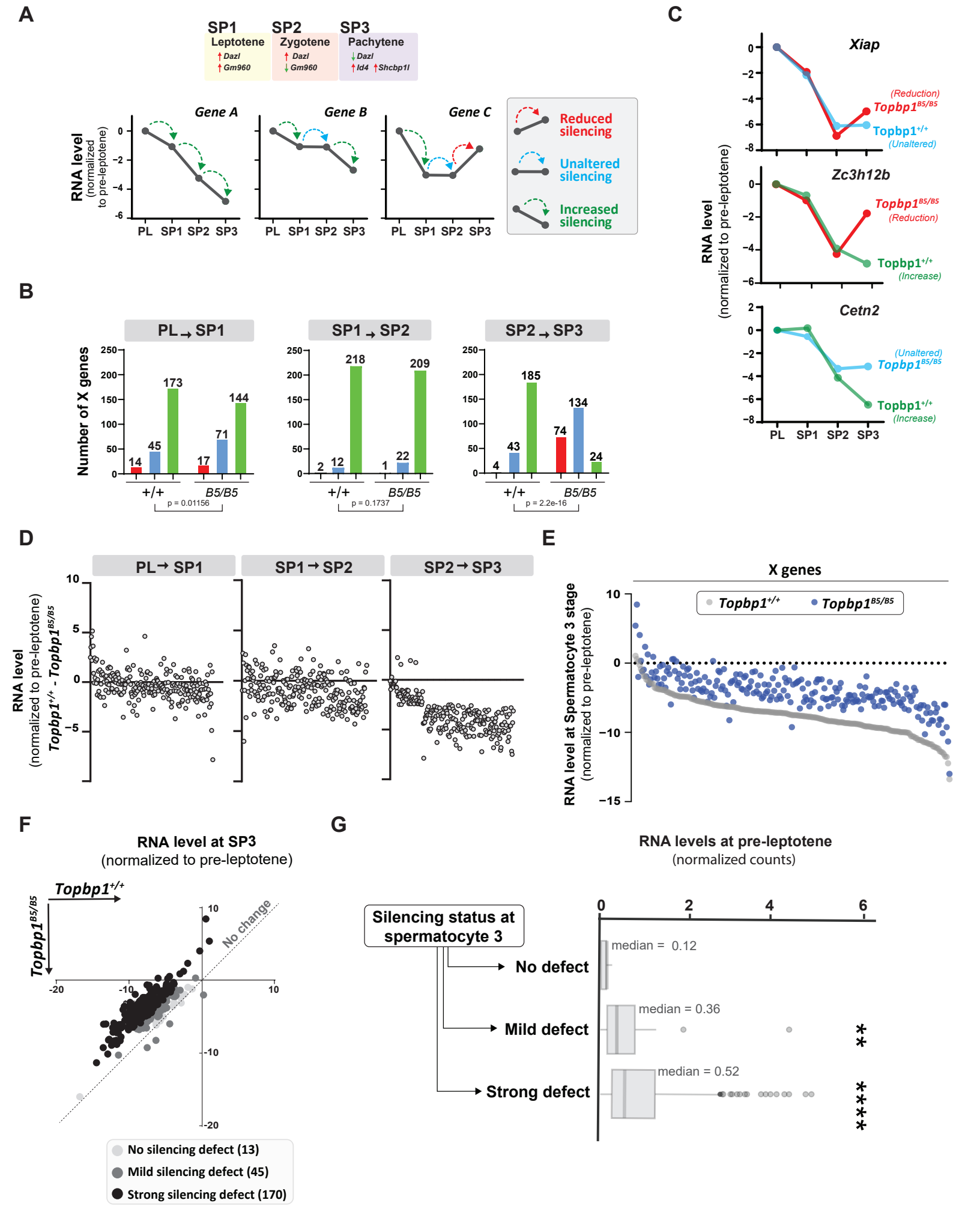
A
SP1 Leptotene
Dazl
Gm960
SP2 Zygotene
Dazl
Gm960
SP3 Pachytene
Dazl
Id4
Shcbp1l
Gene A
Gene B
Gene C
RNA level (normalized to pre-leptotene)
PL SP1 SP2 SP3
Reduced silencing
Unaltered silencing
Increased silencing
B
PL→SP1
SP1→SP2
SP2→SP3
Number of X genes
+/+
B5/B5
p = 0.01156
p = 0.1737
p = 2.2e-16
C
Xiap
Zc3h12b
Cetn2
(Reduction)
Topbp1B5/B5
Topbp1+/+
(Unaltered)
(Increase)
RNA level (normalized to pre-leptotene)
D
RNA level (normalized to pre-leptotene)
Topbp1+/+ - Topbp1B5/B5
E
X genes
Topbp1+/+
Topbp1B5/B5
RNA level at Spermatocyte 3 stage (normalized to pre-leptotene)
F
RNA level at SP3 (normalized to pre-leptotene)
Topbp1+/+
Topbp1B5/B5
No change
No silencing defect (13)
Mild silencing defect (45)
Strong silencing defect (170)
G
RNA levels at pre-leptotene (normalized counts)
Silencing status at spermatocyte 3
No defect
Mild defect
Strong defect
median = 0.12
median = 0.36
median = 0.52

Figure 8

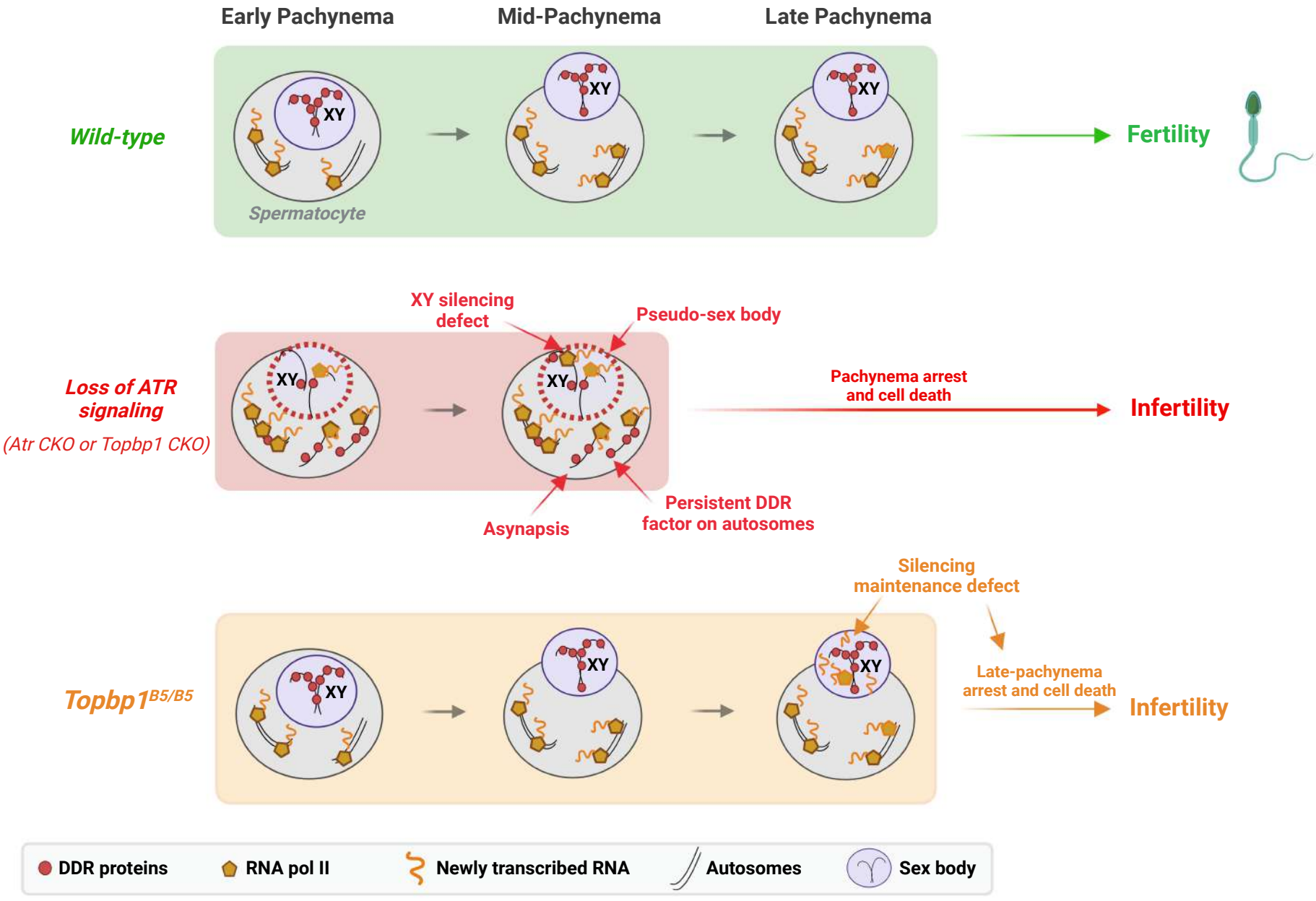
Early Pachynema
Mid-Pachynema
Late Pachynema
Wild-type
XY
Spermatocyte
Fertility
Loss of ATR signaling
(Atr CKO or Topbp1 CKO)
XY silencing defect
Pseudo-sex body
Pachynema arrest and cell death
Infertility
Asynapsis
Persistent DDR factor on autosomes
Topbp1B5/B5
Silencing maintenance defect
Late-pachynema arrest and cell death
Infertility
DDR proteins
RNA pol II
Newly transcribed RNA
Autosomes
Sex body